Alma Mater Studiorum
Università Di Bologna

SCHOOL OF ENGINEERING

-Forlì Campus-

SECOND CYCLE MASTER'S DEGREE in
AEROSPACE ENGINEERING

Class LM-20

GRADUATION THESIS
In Spacecraft Attitude Dynamics and Control

Development and experimental testing of nanosatellites attitude control using mixed magnetic/mechanical actuation

Candidate:
Andrea Curatolo

Supervisor:
Dario Modenini

Co-Supervisor:
Anton Bahu

Academic Year 2020/2021

Abstract

In the last decades, the space sector has seen a constant increase in the number of operating nanosatellites, mainly in the form of CubeSats. Nevertheless, nanosatellites are still characterised by a high failure rate and the importance of ground testing is often underestimated. The Attitude Control System (ACS) is one of the most important subsystems yet one of the least developed for what concerns the CubeSats. Magnetorquers are often employed as main actuators, thanks to their reduced dimensions. However, a spacecraft actuated by magnetorquers alone suffer from an instantaneous underactuation. Reaction wheels offer better performance but are prone to failure and must be desaturated periodically. It's possible to overcome the limits of both types of actuators by employing an ACS equipped with both types of actuators. In this work, an attitude control law integrating three orthogonally placed mangnetorquers and one reaction wheel is studied and experimentally tested on a dynamic simulator.

The first part of the thesis regards the design of the control law. The required control is distributed between actuators using a geometric approach. The control approach is studied through numerical simulations and tuned for a spacecraft of a nanosatellite class. Nonlinear spacecraft dynamical model is considered, as well as worst-case external disturbances, magnetic field and attitude estimation error. The stability of the control law with respect to parameters variations is studied by means of Monte-Carlo approach.

In the second part, the designed control law is validated through Hardware-in-the-loop testing on an attitude simulator testbed developed at the University of Bologna. Before-use facility calibration is described. In particular, to provide almost disturbance-free rotational dynamics, the gravity torque acting on the platform have to be compensated. This is done using a novel approach employing jointly shifting

masses and magnetorquers (responsible for angular velocity damping). Then, the proposed control law is implemented on-board of the simulator and experimentally assessed. The results show high accuracy and robustness with respect disturbances.

Acknowledgements

I would first like to thank Professor Dario Modenini, for giving me the opportunity of working on this thrilling project. Thank you for placing your thrust in me.

A special thanks goes to Dr. Anton Bahu, for his support throughout all the thesis work and for his wise guidance. I will always heed your lessons.

I warmly thank all my friends and colleagues for their esteem and constant encouragement. I feel very lucky to have them by my side.

Finally, thanks to my family, the person I am today is the result of their constant care and support.

Contents

List of Figures

List of Tables

List of acronyms

ABS Automatic Balancing System.

ACS Attitude Control System.

AST Attitude Simulator Testbed.

CM Centre of Mass.

COTS Commercial Off-The-Shelf.

CR Centre of Rotation.

DCM Director Cosine Matrix.

ECEF Earth-Centered/Earth-Fixed.

ECI Earth-Centered-Inertial.

EO Earth Observation.

HC Helmholtz Cage.

HIL Hardware-In-the-Loop.

IGRF International Geomagnetic Reference Field.

IMU Inertial Measurement Unit.

LEO Low Earth Orbit.

LiIO Lithium-Ion.

LQR Linear Quadratic Regulator.

LTI Linear Time-Invariant.

LTV Linear Time Variant.

LVLH Local-Vertical/Local-Horizon.

MED Momentum Exchange Device.

MT Magnetorquer.

P-POD Poly-Picosatellite Orbital Deployer.

PD Proportional Derivative.

PID Proportional Integral Derivative.

SRP Solar Radiation Pressure.

List of Symbols

$\mathcal{F}$	Frame of reference
q	Quaternion
$\mathbf{q}$	Vector component of the quaternion
q_4	Scalar component of the quaternion
$[\mathbf{q}^{\times}]$	Skew symmetric matrix of $\mathbf{q}$
$\boldsymbol{\omega}$	Angular velocity vector $[rad/s]$
$[\boldsymbol{\omega}^{\times}]$	Skew symmetric matrix of $\boldsymbol{\omega}$
$\boldsymbol{\tau}$	Torque vector $[N\ m]$
$\mathbf{u}$	Input vector
$\mathbf{x}$	State vector
y	Output vector
$\mathbf{L}$	Angular momentum vector $[Nms]$
J	Inertia matrix $[Kgm^2]$
μ	Gravitational parameter $[m^3/s^2]$
$\mathbf{R}_s$	Position vector from the center of the Earth
$\hat{n}$	Surface normal unit vector
C_D	Drag coefficient
dA	Surface element
r_{CM}	Center of mass position vector $[m]$
r_{CR}	Center of rotation position vector $[m]$
ρ	Air density $[Kg/m^3]$
Φ	Solar constant $[W/m^2]$
c	Speed of ligth $[m/s]$
$\hat{s}$	Sun direction unit vector $[m]$
C_a	Coefficient of absorption
C_s	Coefficient of specular reflection
C_d	Coefficient of diffusion
$\mathbf{m}$	Magnetic dipole $[Am^2]$

$\mathbf{b}$	Magnetic field $[T]$
∇	Gradient operator
∇^2	Divergence operator
$[\lambda, \theta, \phi]$	Euler angles $[rad]$
$\mathbf{h}$	Wheel angular momentum vector $[Nms]$

1

Introduction

Space exploration and exploitation has brought countless benefits to humanity, whether it be for telecommunication, global positioning, weather forecasting, spin-off technologies or increased knowledge of our solar system. In the beginning, the exploration of space was mainly driven by the governments due to the high cost, complexity and requirement for technically advanced and expensive capabilities. The few examples of privates launching satellites into space were mainly represented by radio amateurs [4]. In recent years, the advent of private companies and the spread of microelectronics resulted in both a reduction in the launching and developing cost and a decrease in the satellites' size. Small satellites are indeed characterized by a short development cycle and low cost if compared to larger satellites. This fact is mainly attributed to the adoption of up-to-date Commercial Off-The-Shelf (COTS) components and to smaller and more agile teams ([4], [5], [6]). Satellites are usually divided into categories according to their dimensions, mass or the type of mission that they should fulfil. A widely accepted classification for the satellites based on the wet mass is reported in Table 1.1.

The number of operating **nanosatellites** has increased in recent years and it is predicted to further increase, as shown in Fig. 1.1. Undeniably, one factor that has contributed to their success is the invention of the CubeSat. Born with the intent of being low-cost and

Class	**Sub-Class**	**Mass** (Kg)
Large satellites		> 1000
Medium satellites		500 to 1000
Small satellites	Minisatellites	100 to 500
	Microsatellites	10 to 100
	Nanosatellites	1 to 10
	Picosatellites	0.1 to 1

Table 1.1: Classification of satellites according to their wet mass

fast to be developed [7], the CubeSats have become extremely popular thanks to their standardization, their modularity and the adoption of standard deployment mechanisms [4]. CubeSats are miniaturized satellites with standardized sizes of one-unit (1U, 10x10x10 mm), or a multiple of one unit (e.g. 3U) [8]. Fig 1.2 shows the Colorado Student Space Weather Experiment (CSSWE) Cubesat prior to integration together with the Poly-Picosatellite Orbital Deployer (P-POD).

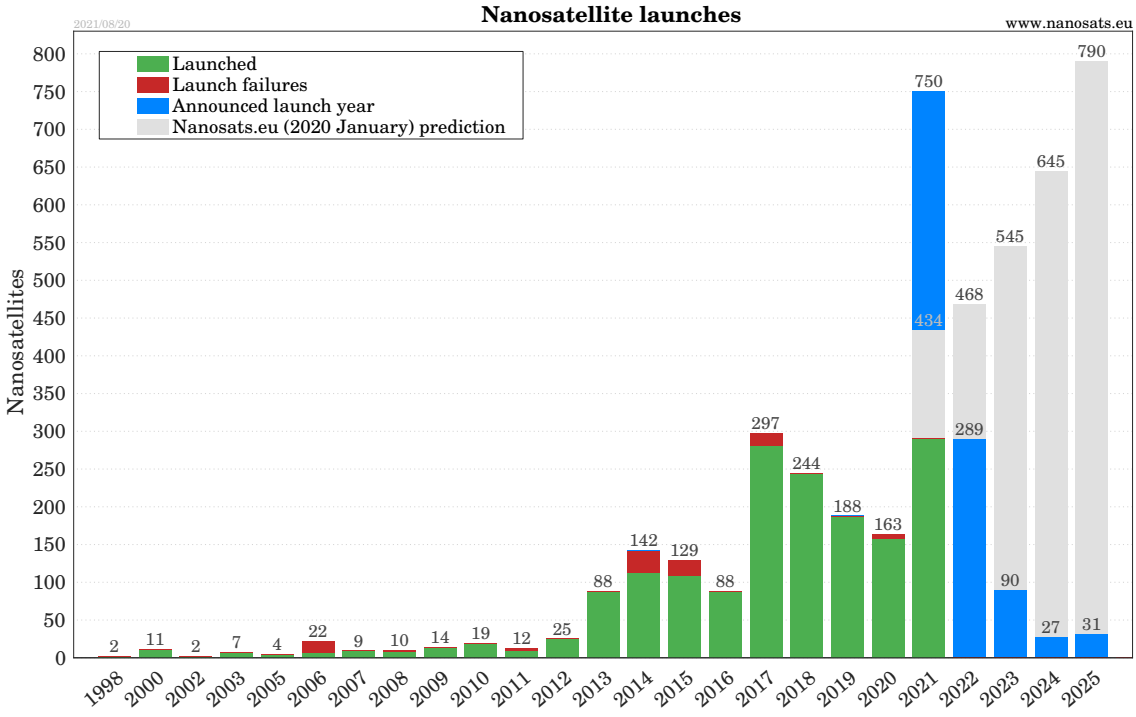

Figure 1.1: Nanosatellites by launch years [1]

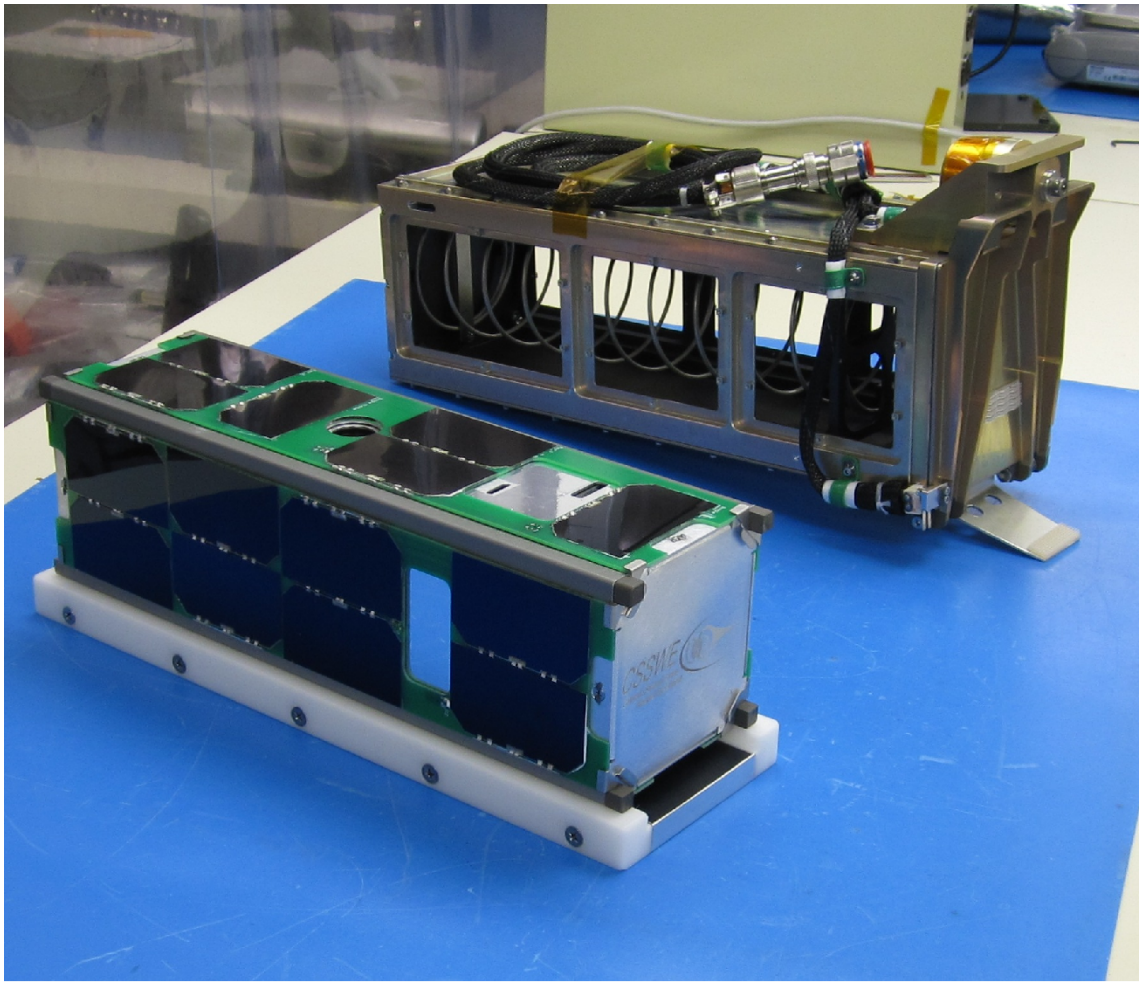

Figure 1.2: CSSWE CubeSat P-POD Deployer prior to integration [2]

Despite their numerous advantages, small satellites are still characterized by a high failure rate. Excluding launch failures, about 20% of Cubesats fails in the early stage of life [5]. The reason for this has been attributed to underestimation of the importance of integrated spacecraft-level systems testing, with teams instead focusing mainly on design and test of the subsystems of the satellite [4]. Hardware-In-the-Loop (HIL) tests are therefore required for proper validation and integration of the satellite subsystems.

The Attitude Control System (ACS) is one of the most important subsystems of a satellite since it allows its nominal orientation in space while counteracting external disturbances. Nevertheless, it is yet one

of the least developed subsystems for what concerns the CubeSats [6]. In the perspective of integrated HIL testing, the ACS is one of the most challenging subsystems to be tested since it requires free-rotational movement in a torque-free environment. Since the beginning of the space age, numerous on-ground spacecraft simulators have been developed, most of them based on air-bearings [3]. The testing facilities normally used for big satellites are inadequate for small satellites due to the unacceptable level of residual disturbance torques [9]. Hence, companies and universities have developed Attitude Simulator Testbeds (AST) tailored for small satellites. In particular, the AST developed at the University of Bologna allows the testing of CubeSats of "1U" and "3U" formats under low torque conditions [10].

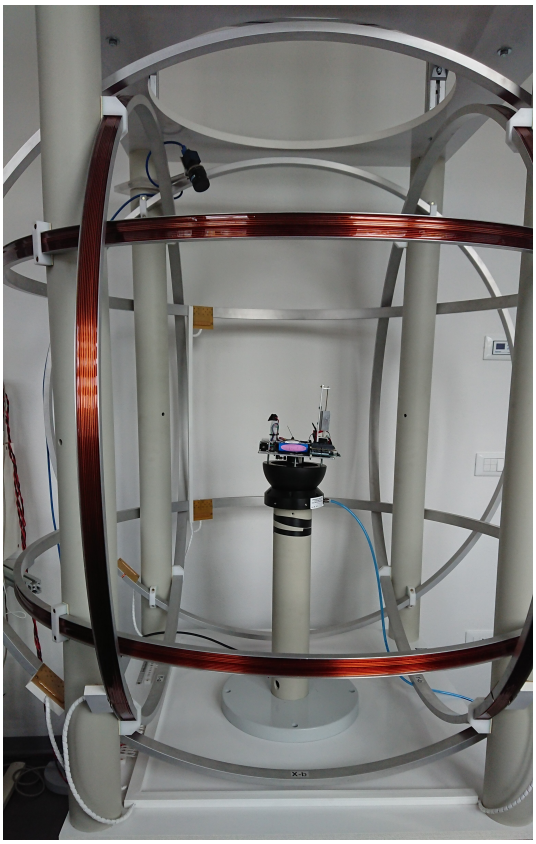

Figure 1.3: The attitude simulator testbed at the University of Bologna with a 1U Cubesat mounted on it

The pointing requirements for a CubeSats may vary depending on

the mission type, with most Earth Observation (EO) missions using active control systems to fulfil strict pointing requirements and most communication missions using passive control systems and relying on omnidirectional antennas to maintain communication with the ground [6]. Magnetorquers and reaction wheels are by far the most used actuators on nanosatellites [6]. In general, the use of Momentum Exchange Device (MED) such as reaction wheels and momentum wheels, is very effective in achieving high pointing accuracy [6]. However, these kinds of actuators must be desaturated periodically using other kinds of actuators such as thrusters or magnetorquers. Failures of one or more Reaction Wheels is a common issue during the operational life of a satellite. Redundancy is often taken in consideration for big satellite while is almost absent for small satellites due to the constraints on their mass and dimensions [11]. Magnetorquers, on the other hand, are more reliable thanks to the absence of parts in relative movement and, thanks to electronic miniaturisation, they have reduced dimensions that make them a valuable solution for small satellites. Fig. 1.4 shows a commercial solution for a magnetorquer board. The main disadvantage of the magnetorquers is their intrinsic underactuation. Indeed, they cannot provide a torque around a direction parallel to the external magnetic field. Depending on the orbit inclination, this underactuation can be considered to be only instantaneous. Indeed, if the Earth's magnetic field varies as the spacecraft travels in its orbit, then within a certain time span all the directions become available for actuation and the system is controllable, as properly justified in [12][13].

Figure 1.4: ISIS magnetorquer board (Image courtesy of ISIS)

1.1 Motivations and contributions

The use of magnetorquers for attitude control offers numerous advantages, especially for small satellites, but the pointing accuracy achievable is limited [6]. In an effort to overcome these limitations and still maintaining a low level of complexity and cost, it was decided to investigate ways in which magnetorquers can be integrated with other types of actuation. A way to compensate for the under-actuation of the magnetorquers can be pairing them with some sort of passive stabilisation, such as gravity gradient or aerodynamic torque or with a mechanical actuation system such as momentum/reaction wheels or thrusters [14]. When MEDs and magnetorquers are used together, there are different possibilities for their joint use. For small satellites, is interesting the case in which 3 magnetorquers are used together with a single wheel. Indeed, these two systems can be integrated reducing the overall size. In the case the MED is a momentum wheel, one talks about a *bias momentum satellite*. The use of a momentum wheel adds gyro stability to the satellite without requiring all its mass to spin: it can dump disturbance torques providing stability properties [14]. One way to integrate these two systems of actuation is to use them simultaneously for attitude control and wheel desaturation manoeuvres as done using a nonlinear model in [15] and a linear model in [16]. In [15], the spacecraft is equipped with 3 magnetorquers and a momentum

wheel and its attitude is parametrised using a sequence of Euler angles. A linear control law for the magnetorquers and a proportional-derivative like command law for the momentum-bias wheel parallel to the pitch axis are used. The stability is proven using a Laypunov function and simulations proved the robustness of the controller under actuator saturation.

The approach adopted in this work instead consists of the use of three magnetorquers and a reaction wheel. The tandem use of magnetorquers and reaction wheels could extend the torquing capability of the spacecraft and bring to power saving [17]. For example, in [18], after the failure of the pitch reaction wheel, the control around the pitch axis was restored thanks to the use of the magnetic coils. In [16], a time-discrete model of a spacecraft equipped with 3 magnetorquers and 3 reaction wheels is used. A cost index is defined and the time-discrete periodic Riccati equation is solved through an algorithm. The performances are compared with the one of a spacecraft using only magnetorquers. As a result, better pointing accuracy is reached and reaction wheel desaturation is achieved. In this work, a control distribution law based on [19], is adopted. In particular, the required control torque is geometrically distributed between the reaction wheel and the magnetorquers. The reaction wheel provides the torque in the direction parallel to the external magnetic field, given that the wheel axis is not perpendicular to such direction. The magnetorquers provide the remaining part of the torque, lying in the plane perpendicular to the magnetic field direction. If the wheel axis and the Earth's magnetic field direction are not perpendicular, three-axis control is achieved. In this work, the control torque is calculated using a Linear Quadratic Regulator (LQR) based on a Linear Time-Invariant (LTI) model for the spacecraft dynamics. To the best of the author's knowledge, this is the first time that the approach introduced in [19] is used with in conjunction with linear control techniques.

The proposed attitude control law was validated with respect to pa-

rameters variations by means of Monte-Carlo approach using *Simulink®*. It was then tuned to be tested hardware-in-the-loop on the AST at the University of Bologna. Prior to the system testing, the disturbance torques affecting the platform had to be compensated. The main torque acting on it is the gravity torque, caused by the misalignment between the Centre of Mass (CM) and the Centre of Rotation (CR) of the platform. Its compensation requires the use of an Automatic Balancing System (ABS), consisting of three motor-driven balancing masses. As a further contribution of this work, the ABS was integrated with the magnetorquers, which provided angular speed damping with reduced vibration. The proposed approach provides better disturbance reduction and ACS performance gain. The designed control law was next implemented on the CubeSat simulator within the AST. Experimental testing showed that the use of mixed magnetic/mechanical actuation is effective in providing high accuracy in three-axis attitude control.

1.2 Outline

In Chapter 2 the theoretical and mathematical description of the control problem and of the experimental facility are provided. In the Chapter 3 attitude control methods for spacecraft employing magnetorquers or MED are summarized. In Chapter 4 developed control law is presented and validated with respect to parameters variations by means of Monte-Carlo approach using *Simulink®*. In Chapter 5 the mass balancing procedure is presented together with the results of experimental tests carried out on the attitude simulator testbed. In Chapter 6 the results of the experimental tests of the mixed magnetic/mechanical control are presented.

2

Preliminaries

In this chapter, the theoretical and mathematical tools that provide the necessary background to address the topics of this work are provided. In section 2.1 the frames of reference commonly used for the attitude determination and control are summarized. In section 2.2 and 2.3, the equations describing the attitude of a rigid body and its evolution in time are addressed, while in section 2.4 the equations describing the attitude dynamics are presented. In 2.5 a short overview of the disturbances torques acting on a satellite is reported. In section 2.6, the attitude simulator testbed at the University of Bologna is described. Finally, in section 2.7 the main control design methods used in this work are summarized. For what concerns the section going from 2.1 to 2.5, [20] was used as the main reference, while section 2.6 is mainly based on the work of [9] and [10].

2.1 Frames of reference

Describing the attitude of a rigid body consists in representing the relative orientation of two different frames of reference. One frame is attached to the rigid body while the other is usually defined by some celestial body. In the case of Earth-orbiting satellites, some frames of reference are of particular interest.

The **body-fixed** reference frame is attached to the spacecraft. Its

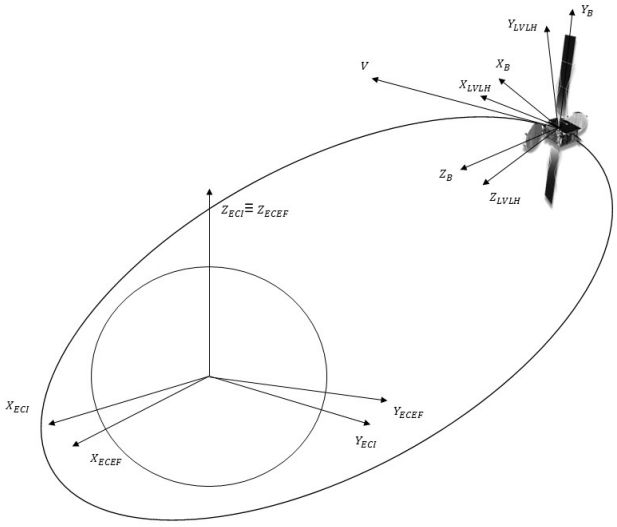

Figure 2.1: Graphical representation of a spacecraft orbiting around Earth together with the frame of reference and the spacecraft velocity vector

origin is placed in the spacecraft CM while the orientation of the axis is arbitrary. Nevertheless, it is a common choice to align the axis to the principal axis of inertia of the spacecraft.

The **Earth-Centered-Inertial (ECI)** is a frame of reference with origin in the Earth centre and translating with Earth. The first axis is aligned with the vernal equinox (whose direction is given by the intersection between the Earth's equatorial plane and the ecliptic plane), the third axis is aligned with the Earth's spin axis pointing north while the second axis comes from the right-hand rule. This frame of reference is pseudo-inertial since the direction of the axis is fixed in space but the origin of them moves with the Earth's revolution around the sun.

The **Earth-Centered/Earth-Fixed (ECEF)** frame of reference differs from the ECI for the definition of the first and second axis. These still lie in the equatorial plane but are directed towards fixed points on the Earth's surface. In particular, the first axis is directed

toward the Greenwich meridian, while the second axis comes from the right-hand rule. As a consequence, the ECEF frame is not inertial as both its origin and the direction of its axis are not fixed.

The **Local-Vertical/Local-Horizon (LVLH)** frame has origin in the spacecraft centre of mass and is of practical interest for many Earth orbiting spacecrafts. The third axis is directed along the nadir, the first axis along the direction of the spacecraft velocity and the second axis is perpendicular to the spacecraft orbit and follows the right-hand rule.

2.2 Attitude representation

The main task of an attitude control system is to orient the spacecraft body frame towards a fixed orientation (*regulation*) or to follow a defined time-varying trajectory (*tracking*). In both cases, the attitude of the spacecraft has to be described using some mathematical parameters.

The most used attitude representation are the **Director Cosine Matrix (DCM)**, the **axis plus angle**, the **sequence of Euler angles** and the **quaternions**. Each representation has advantages and disadvantages in terms of the computational effort, the linearity of the equations and the presence of singularities. Euler angles are widely used for their ease of visualisation but they depend on the particular rotation sequence chosen and each sequence presents a singularity for certain angles. The use of unit quaternions, on the other side, offers a minimum attitude representation without singularities and they are already available from the attitude determination. In this work, both Euler angles and quaternions have been used for parametrizing the attitude and are reported here together with the director cosine matrix.

2.2.1 Director cosine matrix

Given two reference frame, $\mathcal{F}$ and $\mathcal{F}'$, a vector $\mathbf{x}$ has representation respectively $\mathbf{x}_F$ in $\mathcal{F}$ and $\mathbf{x}_{F'}$ in $\mathcal{F}'$. The Director Cosine Matrix A is an orthogonal matrix mapping $\mathbf{x}_F$ to $\mathbf{x}_{F'}$ through Eq. 2.1

$$\mathbf{x}_{F'} = A\mathbf{x}_F \tag{2.1}$$

Since A is orthogonal, it follows that also the following equation holds:

$$\mathbf{x}_F = A^T\mathbf{x}_{F'} \tag{2.2}$$

When the vector $\mathbf{x}$ is a position vector in the three-dimensional space, the DCM A is a 3x3 matrix. It is characterised by 9 parameters satisfying 6 orthogonality constraints.

2.2.2 Euler angles

The Euler angle representation expresses a rotation between two frames of reference as the product of three rotations around three coordinate axes, solidary with the moving body (*intrinsic rotation*). Several combinations of sequences of rotation are possible and are distinguished in *symmetric sequences*, where the first and the last rotation are performed around the same axis, and *asymmetric sequences*, where the rotations are performed around three distinct axes. In this work, the asymmetric sequence 321 was used, with the common notation of *yaw* ψ indicating the rotation around the third axis, *pitch* θ indicating the one around the second axis and *roll* ϕ indicating the rotation around the first axis. The Euler angles representation depends on the particular sequence of rotations used but, in the hypothesis of small angles, the dependency is only on the axis around which the rotations are performed.

2.2.3 Quaternions

A quaternion is a four-component vector with some additional operations defined on it. *Unit quaternions* $q = \begin{bmatrix} q_1 & q_2 & q_3 & q_4 \end{bmatrix}^T$ are used to parametrize rotations. It can be shown that the quaternion can be divided into two parts: the first three components $\mathbf{q}$ (or the last three depending on the convention used) form a vector, strictly related to the instantaneous axis of rotation, while the remaining scalar component q_4 is the cosine of the angle of rotation around the aforesaid axis. Quaternions are related to the DCM by the following equation:

$$A(q) = (q_4^2 - \|\mathbf{q}\|^2)I_3 - 2q_4[\mathbf{q}^\times] + 2\mathbf{q}\mathbf{q}^T \tag{2.3}$$

They are more efficient than the DCM since they consist of only 4 parameters rather than 9 and satisfying only 1 constrain (unit norm) rather than 6 (orthogonality constraints). Also, they don't present singularity in the attitude kinematics, differently from the Euler angles. Often for attitude control, the *reduced quaternion* representation is used. The reduced quaternion representation considers only the vector component of the quaternion and offers some advantages, described in Section 2.7, with the main drawback of introducing a singularity in the representation.

2.3 Attitude kinematics

The attitude kinematics describes the evolution in time of the attitude of a rigid body. It links the time derivative of an attitude representation with the body angular rate $\boldsymbol{\omega}$. If the Euler angles are used, the singularity that arises cannot be overcome while no singularity is present for the quaternion representation. The equations of the attitude kinematics can be derived through differentiation of the attitude representation equation. The kinematics equations for the Euler angles representation depend on the rotation sequence chosen

and are not presented here for brevity. The set of equations for the quaternion attitude kinematics is:

$$\dot{q} = \frac{1}{2}\Omega q \tag{2.4}$$

where Ω is a matrix that contains the components of the body angular rate. The kinematics equations can be rewritten considering separately the the vector component of the unit quaternion $\mathbf{q} = \begin{bmatrix} q_1 & q_2 & q_3 \end{bmatrix}^T$ and the scalar one q_4:

$$\begin{cases} \dot{\mathbf{q}} = -\frac{1}{2}\boldsymbol{\omega} \times \mathbf{q} + \frac{1}{2}q_4\boldsymbol{\omega} \\ \dot{q}_4 = -\frac{1}{2}\boldsymbol{\omega}^T\mathbf{q} \end{cases} \tag{2.5}$$

One can then rearrange the equations to write the time derivative of $\mathbf{q}$ as a function of only $\mathbf{q}$ and $\boldsymbol{\omega}$, leading to the reduced quaternion representation for the attitude kinematics. In this way, the time evolution of $\mathbf{q}$ is only a function of $\boldsymbol{\omega}$ and of $\mathbf{q}$ itself.

$$\dot{\mathbf{q}} = \mathbf{g}(q_1, q_2, q_3, \boldsymbol{\omega}) = \frac{1}{2}\begin{bmatrix} \sqrt{1-q_1^2-q_2^2-q_3^2} & -q_3 & q_2 \\ q_3 & \sqrt{1-q_1^2-q_2^2-q_3^2} & -q_1 \\ -q_2 & q_1 & \sqrt{1-q_1^2-q_2^2-q_3^2} \end{bmatrix}\begin{bmatrix} \omega_1 \\ \omega_2 \\ \omega_3 \end{bmatrix} \tag{2.6}$$

2.4 Attitude dynamics

Euler's rotational equations describe the evolution in time of the angular momentum $\mathbf{L}$ of a rigid body in the body axis frame:

$$\dot{\mathbf{L}} = J\dot{\boldsymbol{\omega}} = \boldsymbol{\tau} - \boldsymbol{\omega} \times (J\boldsymbol{\omega}) \tag{2.7}$$

J is the inertia matrix, $\boldsymbol{\tau}$ is the external torque applied to the spacecraft and $\boldsymbol{\omega} \times (J\boldsymbol{\omega})$ is the gyroscopic coupling. All the quantities are expressed in body frame, $\boldsymbol{\omega}$ is calculated with respect to the inertial

frame. The external torque can be split in the contribution of the disturbance torques and of the control torques.

2.5 Disturbance torques acting in space

The disturbances torques are unintended internal or external torques acting on the spacecraft. Their relative importance depends on the orbit (mainly altitude and inclination), on the shape of the spacecraft, its mass distribution and on the placement of the electronic components. The modelling of these torques is important for the design of the spacecraft attitude determination and control systems. Internal disturbance torques can be caused by the exchange of angular momentum between components of a spacecraft, they include torque due to flexibility and due to the sloshing phenomenon. External disturbance torques arise from the interaction of the spacecraft with the external environment. They include the *gravity gradient torque*, the *aerodynamic torque*, the *solar radiation pressure torque* and the *magnetic torque*. In this work, only external torques have been considered, since the internal torques are usually negligible for nanosatellites because of their reduced dimensions.

2.5.1 Gravity gradient torque

The gravity gradient torque acts on every object with nonsymmetrical mass distribution in a non-uniform gravitational field. It can be explained intuitively in this way: the portion of the object that is more distant from Earth perceive a weaker gravitational attraction compared to the portion nearer Earth. These forces are balanced only for certain configurations of the body, otherwise, they cause a torque around the centre of mass. This torque is negligible for application on or near the Earth's surface, where other torques are much stronger and friction is omnipresent, but it can become important in orbit applications. Considering that the spacecraft mass is much smaller than the Earth's

one and that the distance between these two is much higher than the spacecraft dimensions, an analytical expression for the gravity gradient torque can be derived:

$$\boldsymbol{\tau}_{gg} = \frac{3\mu}{R_s^3}\hat{\mathbf{R}}_s \times (J\hat{\mathbf{R}}_s) \tag{2.8}$$

where μ is the gravitational parameter, $\mathbf{R_s}$ is the vector going from the centre of the Earth to the spacecraft centre of mass and J is the inertia matrix. It is clear from this expression that the magnitude of the torque decreases with the distance to the cube power. It is also evident that no gravity gradient torque is present whenever a principal axis of inertia is aligned with the local vertical direction. If one then considers the dynamics of a spacecraft orbiting around Earth, he discovers that for a circular orbit where all the 3 principal axes of inertia are aligned with the axes of an orbit frame, the gravity gradient torque provides three-axis stabilisation. For a sub-circular orbit, that is more probably the case of a real orbit, the system is stable if the inertia matrix of the spacecraft satisfies some proprieties [21].

Thanks to its analytical expression, the gravity gradient is the easiest torque to be modelled and for this reason, it is often considered not only in the test phase of a controller but also in its design phase.

2.5.2 Aerodynamic torque

Even in space application, the Earth's atmosphere can play an important role on spacecraft dynamics. At this altitude, the behaviour of the atmosphere is strongly influenced by the solar activity and the atmospheric density can vary by several order of magnitude during the years [22]. The interaction of the atmosphere with a surface at this altitude can be described by plastic impacts, with particles loosing their entire energy on collisions with the satellite [23]. The expression for the aerodynamic torque is:

$$\boldsymbol{\tau}_a = \int_A \mathbf{r} \times [-\frac{1}{2}\rho C_D v^2 (\hat{\mathbf{v}} \cdot \hat{\mathbf{n}})] dA \tag{2.9}$$

where $\mathbf{v}$ is the relative velocity of the spacecraft with respect to the atmosphere, $\hat{\mathbf{n}}$ is the unit vector normal to the surface dA and $\mathbf{r}$ is the position vector of with respect to the centre of the spacecraft. C_D is the drag coefficient and for practical applications, it can be set to 2.0 if no measured value is available [21]. Often, this expression is simplified by considering the spacecraft as the sum of simpler surfaces such as flat surfaces and taking into account only the surfaces for which the angle between the relative velocity and the unit normal to the surface is less than 90 deg. As a first approximation, one can consider the largest surface and a distance between the centre of pressure and the centre of mass. In that case, the norm of the torque vector becomes:

$$|\boldsymbol{\tau}_a| = \frac{1}{2}\rho S C_D v^2 |C_p - C_m| \tag{2.10}$$

One common assumption consists in considering the atmosphere as co-rotating with the Earth, thus making v the velocity relative to the Earth's surface.

2.5.3 The solar radiation pressure torque

Photons carry momentum and this can be exchanged with a solid surface. For the Solar Radiation Pressure (SRP), mainly three types of interaction between light and a surface are considered: fully absorption, specular reflection and diffusive reflection (transmission is usually negligible). For each type of interaction, it is defined a coefficient c expressing the fraction of momentum flux interesting each phenomenon. The solar radiation pressure torque is thus described by:

$$\boldsymbol{\tau}_{srp} = \int_A \mathbf{r} \times \{-\frac{\Phi}{c} cos(\alpha)[(c_a + c_d)\hat{\mathbf{s}} + (2cos(\alpha)c_s + \frac{2}{3}c_d)\hat{\mathbf{n}}]\} dA \tag{2.11}$$

where Φ is the power flux, c is the speed of light, α is the angle between the normal to the surface element $\hat{\mathbf{n}}$ and the sun direction $\hat{\mathbf{s}}$. Also in this case, the spacecraft can be decomposed into simpler shapes. As a first approximation, one can consider the largest surface, a distance between the centre of pressure and the centre of mass and the sun direction to be coincident with the normal direction, i.e $\alpha = 90°$. Finally, only two of the three coefficients c are independent since for the conservation of energy their sum is equal to 1. Writing $c_a = 1 - c_d - c_s$ and taking into considerations the other simplifying assumptions, Eq. 2.11 becomes:

$$|\boldsymbol{\tau}_{srp}| = \frac{\Phi}{c} S(1+p)|C_p - C_m| \tag{2.12}$$

where p can be seen as an equivalent coefficient of reflection and for a first approximation it can be set equal to 0.6.

2.5.4 Magnetic torque

The Earth's geomagnetic field can interact with the spacecraft to produce various kind of torques. For non-rotating spacecrafts the most important torque is the one that arises when a magnetic dipole $\mathbf{m}$ is immersed in an external magnetic field $\mathbf{b}$ [21]:

$$\boldsymbol{\tau}_{mag} = \mathbf{m} \times \mathbf{b} \tag{2.13}$$

For Earth's orbiting spacecraft the external magnetic field coincides with the Earth's magnetic field. Since the absence of surface electric currents, the Earth's magnetic field can be expressed as the gradient of a scalar potential, V:

$$\mathbf{b} = -\nabla V \tag{2.14}$$

and since the absence of magnetic monopole, the scalar potential V satisfies the Laplace's equation:

$$\nabla^2 V = 0 \tag{2.15}$$

The solution to this equation is expressed conveniently in spherical harmonics:

$$V(r,\theta,\phi) = a\sum_{n=1}^{k}(\frac{a}{r})^{n+1}\sum_{m=0}^{n}(g_n^m cos(m\phi) + h_n^m sin(m\phi))P_n^m(\theta) \quad (2.16)$$

where a is the equatorial radius of the Earth; g_n^m and h_n^m are called *Gaussian coefficients*; r, θ, and ϕ are the geocentric distance, coelevation, and east longitude from Greenwich; and $P_n^m(\theta)$ are the associated *Legrendre functions*. For practical purposes, the sum is truncated at some degree and the error made in the truncation depends on the distance from the Earth's surface [21]. The Gaussian coefficients are determined experimentally by combining Earth-based and satellite measurements of the geomagnetic field and are grouped in the International Geomagnetic Reference Field (IGRF). The main contribution to the sum is given by the term of degree 1, namely the dipole. One can take advantage of this fact and approximate the magnetic field as the one created by a vector dipole $\mathbf{m}$ (to not be confused with the dipole created on board). Its expression is given by [21]:

$$\mathbf{b}(\mathbf{R}) = \frac{a^3 H_0}{R^3}[3(\hat{\mathbf{m}}\cdot\hat{\mathbf{R}})\hat{\mathbf{R}} - \hat{\mathbf{m}}] \quad (2.17)$$

where $\mathbf{R}$ is the position vector of the point at which the field is desired and H_0 can be evaluated as [24]:

$$H_0 = \frac{4\pi}{\mu_0}\sqrt{(g_1^0)^2 + (g_1^1)^2 + (h_1^1)^2} \quad (2.18)$$

Eq. 2.17 offers the advantage that $\mathbf{b}$ can be evaluated in any convenient coordinate system by expressing $\hat{\mathbf{m}}$ and $\hat{\mathbf{R}}$ in that coordinate system. Fig. 2.2 compares the full IGRF model and the dipole approximation for an orbit inclination of 0 deg.

A magnetic dipole can be present on the spacecraft because of open loops created by the electric cables. A good design of the electric

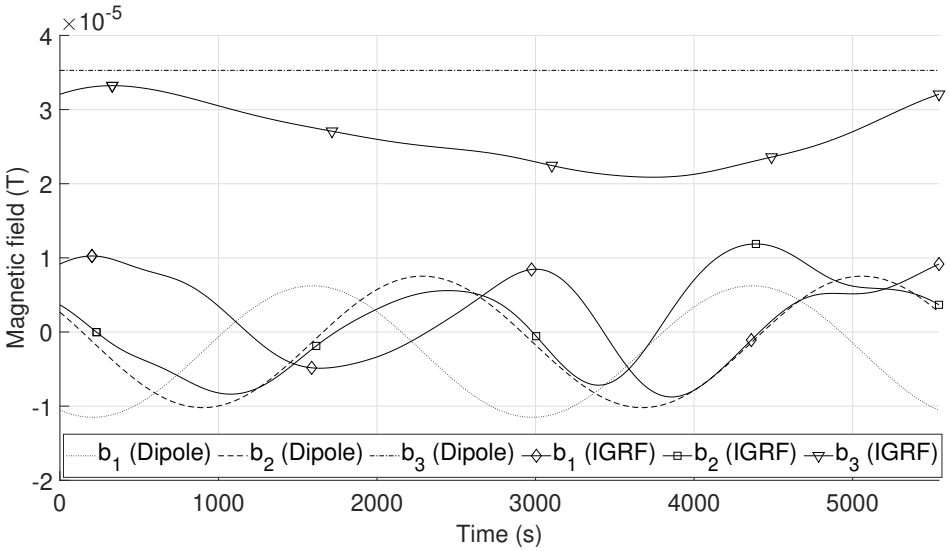

Figure 2.2: Comparison of the full IGRF model (IGRF) and its dipole approximation (Dipole) for an orbit inclination of 0 deg.

wiring should avoid its presence but practically a residual magnetic dipole will always be present on board. Depending on the size of the spacecraft and on its altitude, this torque can be the predominant one. At the same time, this physical phenomenon can be used as a way to provide an active control torque. This is done by creating on board a magnetic dipole in such a way that the torque arising from the interaction with the Earth's magnetic field can be used to control the attitude of the spacecraft. This kind of control suffers from an instantaneous underactuation since the torque will always be in the plane perpendicular to $\mathbf{b}$.

2.6 Attitude simulator testbed

The importance of an adequate ground verification process is often underestimated in the development and test of a nanosatellite. This requires the testing of the satellite in an environment that is as close as possible to the one encountered in space. When it comes to the testing of the ACS, it is essential to provide a free rotational motion in

a low torque environment. To do so, one common solution consists of an air bearing system. This can be used to enable rotational motion, translational motion or both. In the case of rotational motion solely, the air bearing system constrains the structure to rotate around a fixed point, the Centre of Rotation (CR), that in general doesn't coincide with the Centre of Mass (CM) of the moving part. This misalignment generates a gravity torque, that must be compensated through some mass balancing system. Depending on the mission, it could be required to simulate also the magnetic field, sunlight, starry sky, infrared Earth [10]. The AST at the University of Bologna includes an air bearing system, an Automatic Balancing System (ABS) and a Helmholtz Cage (HC) to simulate the magnetic field. It includes also a Sun simulator and a ground truth vision system that, however, were not used in this work.

In section 2.6.1 the Helmholtz cage is described, while 2.6.2 regards the air bearing platform. Finally, in 2.6.3 the hardware architecture of the satellite is described.

2.6.1 Helmholtz cage

A Helmholtz cage is based on the use of three orthogonal Helmholtz coils. A Helmholtz coil consists of a pair of coils, one parallel to each other, each one including N wrapping. When a coil with radius a is traversed by a current I it generates a magnetic field according to Eq. 2.19 [25].

$$b = \frac{32\pi NI}{5\sqrt{5}a} \times 10^{-7} \tag{2.19}$$

The generated magnetic field is uniform within a certain region, whose extension depends on the radius of the coil. Using three orthogonal Helmholtz coils allows generating a magnetic field with arbitrary direction in space. The HC used is a Ferronato® BH-1300-3-C from Serviciencia, Toledo, Spain. It has coils of 1300mm of diameter and

is capable of generating an arbitrary magnetic field in the range ±10 gauss (1 gauss = 10^{-4} tesla) with in-homogeneity below 1% in a spherical volume of 404 mm in diameter, concentric with the coil pairs. Its accuracy in tracking a time-varying magnetic field was enhanced via a closed-loop control system employing a fluxgate magnetometer (AP539, from Applied Physics Systems, Mountain View, CA, USA) [10]. The Helmholtz cage can be used to compensate for the magnetic field present in the laboratory and to simulate a desired magnetic field.

2.6.2 Air bearing platform

Air bearing platforms consist of a grounded and a moving part whose relative motion is characterized by very low friction. The grounded part is provided with small holes where pressurized air passes through, creating a thin film that is needed to support the weight of the moving part and at the same time lubricates the kinematic coupling. The use of spherical bearing provides in theory unconstrained rotational motion but most of the time the motion is constrained for reasons of practical realization of the platform (an example of unconstrained rotational motion is provided in [8]). Spherical air bearing platforms are broadly divided into three categories: table-top, umbrella and dumbbell, as shown in Fig. 2.3. Tabletop- and umbrella-style platforms provide unconstrained rotational motion in the yaw axis, but pitch and roll motion (indistinguishable in this type of platform) are typically constrained to angles of less than 90 deg, a dumbbell-style platform instead, provides unconstrained motion in roll and yaw [3]. The air bearing used for this work consisted of an articulated stand (Ferronato® ULTAS-1 from Serviciencia, Toledo, Spain), of a spherical air bearing with a diameter of 150mm by Physical Instrumetns and tabletop-style platform. The simulator is capable of providing full rotational motion in yaw and up to 45 deg in roll/pitch [9].

Ideally, the disturbance torques affecting the platform should be maintained as low as the one found in orbit, i.e in the order of $10^{-5}Nm$.

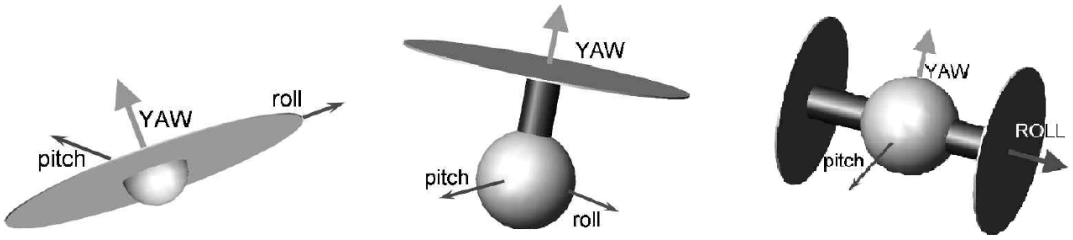

Figure 2.3: Type of air bearings. From left to right: tabletop-style, umbrella-style and dumbbell-style [3]

Values reported in the literature are no lower than $5 \times 10^{-5} Nm$ [9]. Characterization of these torques is thus required. The disturbance torques affecting an air bearing platform can arise from different sources. In [26] the torques affecting an air bearing platform are divided in 4 groups: the *torques arising from the platform*, the *torques from bearing*, the *torques from environment* and the *torques from the test system*. The torques that arise from the platform include the *gravity torque* and the *anisoelasticity*, a torque caused by the deformation of the platform at different tilt angles. In our case, the first is the main torque acting on the platform while anisoelasticity is not a concern because of the reduced dimensions. The torques from the bearing include the *aerodynamic turbine torque*, i.e. the torque caused by the not precisely symmetrical airflow. This is mitigated thanks to the use of high-end COTS components with very low friction. The torques from the environment include the aerodynamic torque, residual dipole torque and vibrations. The aerodynamic torque is neglected due to the small angular velocity and dimensions, the residual dipole torque is minimised using a-magnetic materials for the platform while the vibrations are minimized through robust mounting. The torques from the test environments, such as mass shift in bearing and loose fits, are important in large test platforms while can be neglected in this case [9].

While other torques can be minimised by carefully designing the

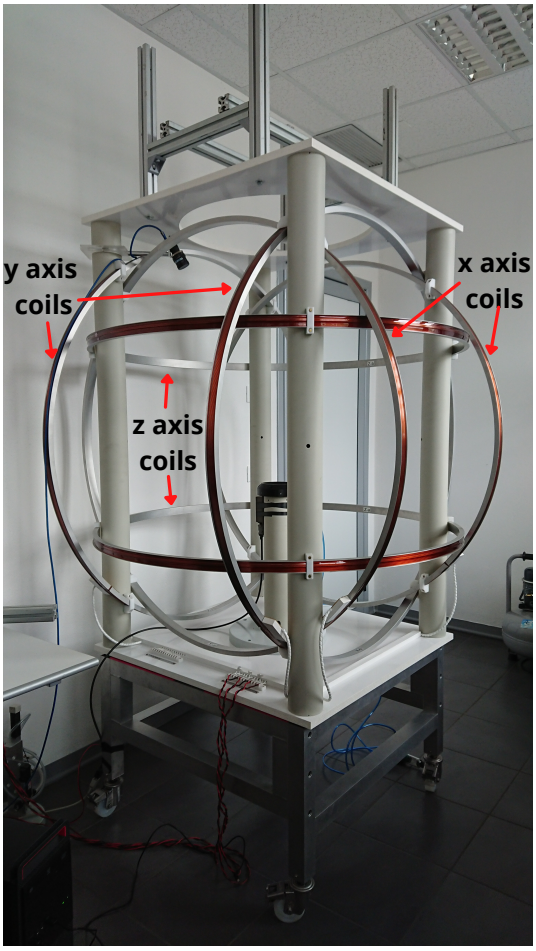

Figure 2.4: The Helmholtz cage of the AST of the University of Bologna with the air bearing semi-emisphere in the centre

test platform, the gravity torque is present whenever there is a misalignment between the CM and the CR of the platform. The distance between these two defines the *unbalance vector*. Theoretically once this is known, the gravity torque can be compensated through mass balancing. Actually, it can be only estimated with finite precision, dictated by the precision of the Inertial Measurement Unit (IMU). Manual balancing procedures can be implemented but they result to be time-consuming and don't guaranty a priori performance level [9],[27]. To overcome these limits, automatic balancing procedures should be used. An automatic balancing procedure requires the determination of the centre of mass position together with the inertia parameters. Their

identification constitute a *dynamic parameter identification problem*, for which different solutions have been proposed in the literature [8]. The air bearing platform at the University of Bologna includes an ABS that utilizes three stepper motors driving three balancing masses, allowing to move the CM within a region that includes the CR. This system is used for fine balancing procedure after a coarse balancing is obtained by components positioning.

2.6.3 Satellite hardware

The on board controller consists of a M0 Feather board by Adafruit, programmed to run different control modes. These range from the balancing feedback algorithm to few attitude control algorithms that make use of the magnetorquers and of the wheel. The IMU used consists of a Xsens MTi-3, which provides angular velocity data, orientation information and magnetic field reading. The sensor specification are reported in table 2.1 while in Fig. 2.5 is shown a picture of the satellite with the main components.

Both the M0 Feather and the Xsens are powered by a 3.6 V Lithium-Ion (LiIO) battery. A 7.2 V LiIO battery powers the three stepper motors, the three magnetorquers and the reaction wheel. Each motor moves a mass of $0.041Kg$ with a minimum step of $2\mu m$. Each Magnetorquer (MT) could provide a maximum dipole of $1Am^2$. The reaction wheel is made up of a flywheel powered by a brushless DC motor (T-Motor Navigator MN1806 1400kv) and is mounted below the main plate, along the satellite z-axis. The characterization of the motor showed a highly nonlinear behaviour at low angular speed. For this reason, the wheel is used as a momentum wheel with low bias rather than as a reaction wheel. This choice implications are explained in Chapter 6.

Attitude determination fusion alghorithm performance	
Roll/Pitch	$0.5°$ RMS
Yaw	$2°$ RMS
Gyroscope	
Standard full range	$\pm 2000°/s$
In-run bias stability	$10°/h$
Bandwidth (-3dB)	$230Hz$
Noise density	$0.003°/s/\sqrt{Hz}$
g-sensitivity (calibrated)	$0.001\%FS$
Accelerometer	
Standard full range	$\pm 16g$
In-run bias stability	$30\mu g$
Bandwidth (-3dB)	$230Hz$
Noise density	$70\mu g/\sqrt{Hz}$
Magnetometer	
Standard full range	$\pm 8G$
Non-linearity	0.2%
Total RMS noise	$0.5mG$
Resolution	$0.25mG$

Table 2.1: IMU specifications

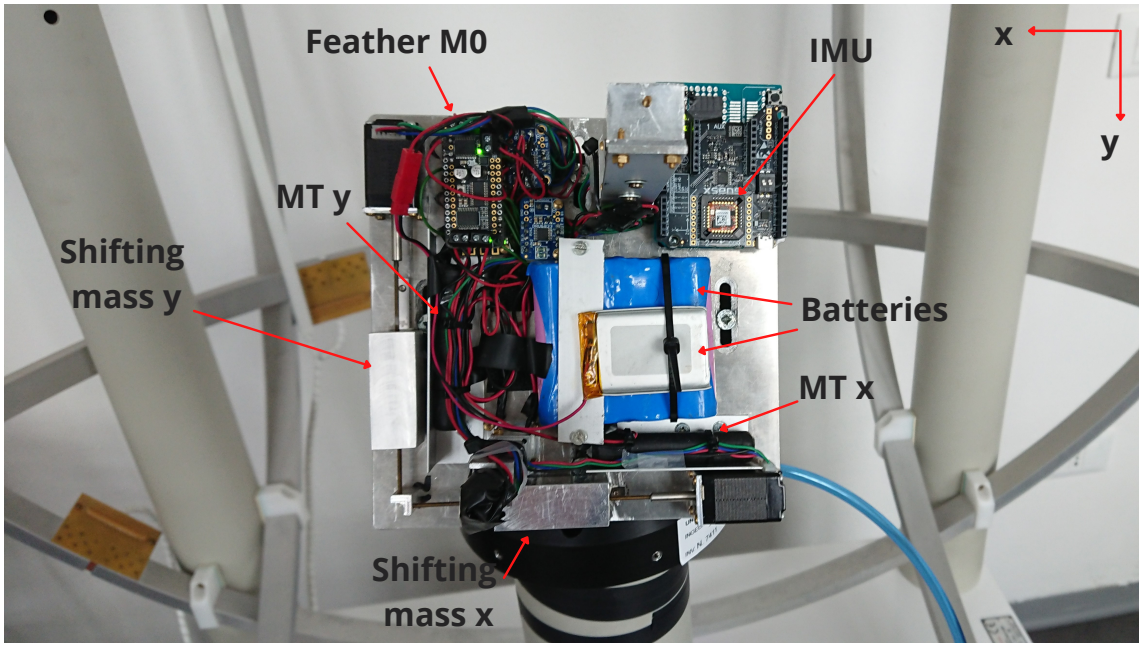

(a)

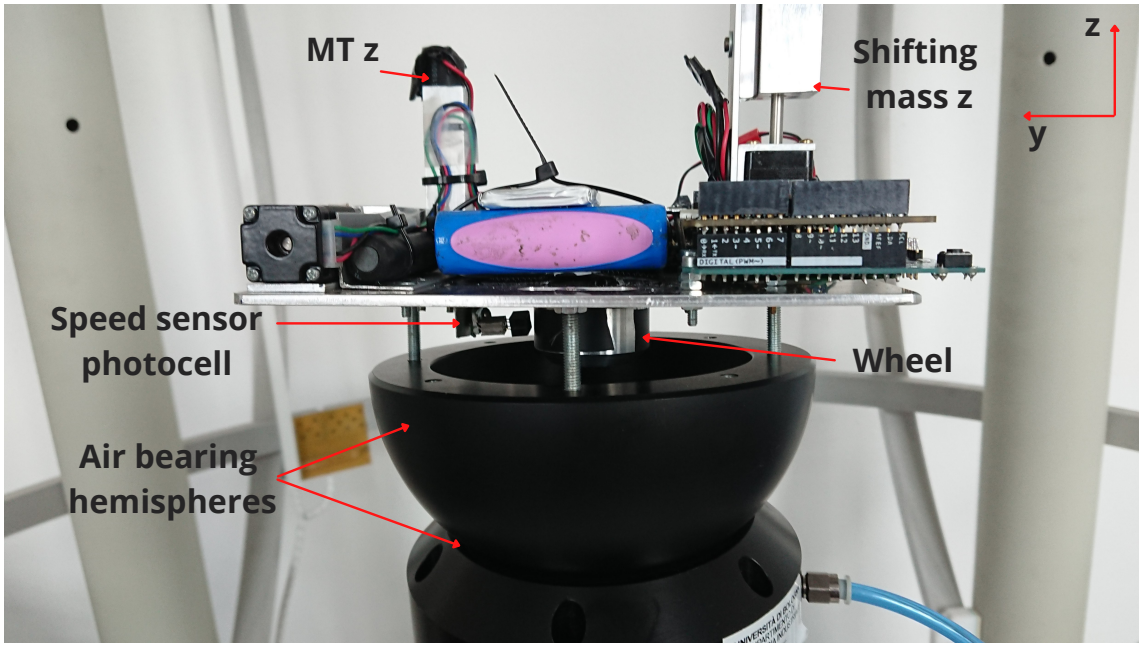

(b)

Figure 2.5: Picture of the satellites with the main components

2.7 Control design methods

There are different methods that can be used to control dynamical systems. These are broadly divided in linear control methods and nonlinear control methods, depending on the model used to describe the system, respectively a linear or nonlinear model. Most dynamical systems are actually nonlinear, such as the one describing the attitude evolution of a spacecraft (see Eq. 2.7 and Eq. 2.6). For nonlinear models, a widely employed method to ensures global asymptotic stability (defined in 2.7.1) consists in the use of the Laypunov second method. Its disadvantage is that it does not address control performances and it is not characterised by a general procedure. Moreover, there is no generalized approach to address external input such as noise and disturbances [28]. The input-output stability framework overcomes this limit of the Lyapunov theory and investigates the relationship between the input and the output of a system. In particular, it considers a system to be stable if bounded input leads to bounded output, where the concept of boundedness has to be specified.

Under certain assumption, it's possible to rely for the control law design on the linear model developed starting from the complete nonlinear model of the system. In some cases a controller designed using a linearised model can be proven, either analytically or experimentally, to stabilise also the original nonlinear system. Developing a linear model allows for the use of well established linear control methods and to an easier evaluation of the controller performances in the neighborhood of the origin. To develop a linear model, one assumes that the system behaves about an equilibrium condition and that it remains close to it. The equations are linearised using a Taylor expansion around the equilibrium condition and the nonlinear terms are neglected. In case Euler angles are used to describe the attitude, the linearised model describing the spacecraft dynamics is controllable but it's not guaranteed in general that the controller designed using the

linear model globally stabilizes the nonlinear system. In other words, the control can become unstable for attitude far from the linearisation point [16]. A linearised model derived using the quaternions it's in general not controllable. To overcome this limit, one can use a reduced quaternion model. This representation has a singular point but for an angle equal to $\pm\pi$ the most distant from the origin, that is the point usually used for the linearisation. At the same time, it offers the advantage that the linearised model is controllable and, under certain conditions, the designed control system globally stabilizes the nonlinear system.

Another important distinction is between time-invariant and time-variant systems. Time-variant systems response to an input depends on the time instant the input is applied, while for time-invariant systems the response is independent of time. A spacecraft using magnetorquers for attitude control constitute an example of time-variant system. Indeed, the control torque is generated from the interaction between the dipole of the magnetorquers and the Earth's geomagnetic field that varies as the spacecraft travels along the orbit. The time-varying nature of the system could be taken into consideration when designing a controller. Time-variant controllers could offer better performances when the system has a strong time-varying nature. This is the case of magnetic control where the Earth's geomagnetic field can be considered to be periodic along the spacecraft orbit. The drawbacks of time-varying controllers are the increase in complexity for what concerns the design and implementation of the controller and the increase in memory occupied on the on board computer. One way to attenuate this problem in the case of Earth orbiting spacecraft is to use the periodic nature of the system by considering the average Earth's magnetic field, as done in ([29],[30],[31])

In this section, the control theory upon which this work is based is recalled. Either if the designed control law is derived using a LTI model of the spacecraft, concepts strictly related to nonlinear control

theory, such as the Lyapunov second method, are often mentioned in the text. For this reason, it was decided to recall such notion in this chapter. Stability of nonlinear systems is addressed in Section 2.7.1. In Section 2.7.2 the Lyapunov second method is presented. In Section 2.7.3 and 2.7.4 respectively the Proportional Integral Derivative (PID) and Linear Quadratic Regulator (LQR) control methods are recalled. In Section 2.7.5 LQR design in case of inertial pointing is considered, for a fully actuated spacecraft with no reference to the type of actuation.

2.7.1 Stability of nonlinear systems

Let's consider the system with state-equation 2.20, which could represent the time evolution of the angular velocity of a rigid body.

$$\dot{\mathbf{x}}(t) = \mathbf{f}(\mathbf{x}(t)) \qquad \mathbf{x}(0) = \mathbf{x}_0 \tag{2.20}$$

where $\mathbf{x} \in \mathbb{R}^n$ and assume the existence of solutions $\mathbf{x}(\mathbf{t})$ to the state-equation in some open set $D \in \mathbb{R}^n$. An equilibrium point is a state of the system $\mathbf{x}_T$ that satisfies $\mathbf{f}(\mathbf{x}_T) = \mathbf{0}$. The equilibrium can be *Lyapunov stable*, *asymptotically stable* or *exponentially stable*. If we consider small perturbation from the equilibrium state, the equilibrium is said to be Lyapunov stable if the perturbed state remains close to the equilibrium point; if in addition, the state converges to the equilibrium in an infinite time then it is said to be asymptotically stable; if in addition, it converges faster or as fast as a given exponential it is said to be exponentially stable. The conditions stated above define local stability, if they are satisfied for whatever initial point and whatever trajectory of the system state (that is $D = \mathbb{R}^n$), then they define global stability.

2.7.2 Lyapunov's second method

Lyapunov's theory covers the stability of nonlinear autonomous systems. The Lyapunov second method defines a necessary and sufficient condition for global asymptotic stability. If one can define a scalar potential function V, also called *extendend energy function*, which is continuous and with a global minimum at the target state $\mathbf{x}_T$, then the state of the system converges to $\mathbf{x}_T$ if and only if the rate of change of the potential, $\dot{V}$, is negative defined. If this doesn't happen, one can design a control action $\mathbf{u}$ such that the forced system satisfies the above condition. The Lyapunov second method suggests a way to design a stabilizing control action. Given a dynamical system:

$$\dot{\mathbf{x}} = \mathbf{f}(\mathbf{x}, \mathbf{u}) \tag{2.21}$$

define a continuous Lyapunov function V that satysfies:

- $V(\mathbf{x}_T) = 0$
- $V(\mathbf{x}) > 0$, for $\mathbf{x} \neq \mathbf{x}_T$
- $V(\mathbf{x}) \to \infty$, for $\mathbf{x} \to \infty$

design a control action $\mathbf{u} = \mathbf{u}(\mathbf{x})$ such that:

$$\dot{V}(\mathbf{x}) = \frac{\partial V}{\partial \mathbf{x}} \frac{d\mathbf{x}}{dt} = \frac{\partial V}{\partial \mathbf{x}} f(\mathbf{x}, \mathbf{u}) < 0, \text{ for } \mathbf{x} \neq \mathbf{x}_T \tag{2.22}$$

The *LaSalle theorem* (valid only for time-invariant systems) extends the result of the Lyapunov second method in the case in which:

$$\dot{V}(\mathbf{x}) \leq 0, \text{ for } \mathbf{x} \neq \mathbf{x}_T \tag{2.23}$$

$$\dot{V}(\mathbf{x}) = 0 \iff \mathbf{x}(t) = \mathbf{x}_T, \forall t. \tag{2.24}$$

The main drawback of the Lyapunov method is that it doesn't exist a procedure to define a Lyapunov scalar function. At the same

time, this allows for flexibility: different Lyapunov functions can be defined for the same dynamical system and multiple control laws can be designed to stabilise the same function.

2.7.3 Proportional Integral Derivative control

Let us consider the following linear system, that could represent the dynamics of a nominally inertially fixed spacecraft around the first axis when small angles and rates are assumed:

$$J_x\ddot{\phi} = u_c + \tau_d \tag{2.25}$$

τ_{xc} is the control torque and τ_{dx} is the disturbance torque. Let's also consider a reference signal r and an output signal $y(t) = \phi(t)$ and let's define the error signal as:

$$e(t) = r - y(t) \tag{2.26}$$

A Proportional Derivative (PD) control consists in providing a control input that is the sum of a scaling of the error signal and of its derivative:

$$\tau_c = K_p e(t) + K_d \dot{e}(t) \tag{2.27}$$

Assuming constant $r(t)$ and zero disturbance torque, the spacecraft equation of motion becomes:

$$J_x\ddot{\phi} = K_p(r - y(t)) - k_d\dot{y} \tag{2.28}$$

that is a spring-mass-damper system. If the reference attitude $r(t)$ is constant and there is no disturbance torque, the error signal will converge to zero and oscillation will be damped. If a constant disturbance torque is added, there will be a steady-state error in the attitude. With the Proportional Integral Derivative (PID) control, an integral term is added to the control law:

$$\tau_{cx} = K_p e(t) + K_d \dot{e}(t) + K_i \int_0^t e(\tau) d\tau \tag{2.29}$$

that will drive the error to zero.

2.7.4 Linear Quadratic Regulator control

Let's recall the linear quadratic optimal control problem with infinite control horizon. Given a linear system in state space representation:

$$\dot{\mathbf{x}} = A\mathbf{x} + B\mathbf{u} \tag{2.30}$$

$$\mathbf{y} = C\mathbf{x} \tag{2.31}$$

and a quadratic cost index L:

$$L = \frac{1}{2} \int_0^\infty (\mathbf{x}^T Q \mathbf{x} + \mathbf{u}^T R \mathbf{u}) dt \tag{2.32}$$

with Q and R positive definite matrices, find a state feedback input

$$\mathbf{u} = -G\mathbf{x} \tag{2.33}$$

such that 2.30 is satisfied and 2.32 is minimised. Minimising the cost index means minimising the deviation of $\mathbf{x}$ from the target state in compromise with the energy spent. The relative importance of these two requirements is tuned by a proper choice of matrices Q and R. Under the assumptions of (A, B) being constant completely controllable, (A, C) constant and completely observable and with the former requirements on Q and R, the solution to the problem is given by:

$$\mathbf{u}(t) = -R^{-1} B^T F \mathbf{x}(t) = -G\mathbf{x} \tag{2.34}$$

with F being the solution of the ARE (Algebraic Riccati matrix Equation):

$$-FA - A^TF + FBR^{-1}B^TF - Q = 0 \tag{2.35}$$

It can be proven that the poles of the system that uses this feedback law have all negative real part, hence stabilizing the system.

2.7.5 LQR Design for inertial pointing spacecraft

Let's consider the case in which the spacecraft has to be oriented with respect an inertially fixed reference . The attitude is parametrised in terms of a reduced quaternion representation, describing the orientation of the body frame with respect to an inertial frame. The reduced kinematic equation is 2.6 and the dynamical equation is 2.7. To derive a linearised model, it is assumed that the attitude of the spacecraft is sufficiently close to the nominal attitude $q_1 = q_2 = q_3 = 0$ ($q_4 = 1$) (body frame aligned with inertial frame) and that the body angular rate is sufficiently close to zero. Sufficiently close means that second and higher-order terms in a Taylor expansion around the linearisation point can be neglected. The dynamic and kinematic equations are linearised and are written in the state space representation. The state of the system is defined as $\mathbf{x} = \begin{bmatrix}\boldsymbol{\omega}^T & \mathbf{q}^T\end{bmatrix}^T$ and $\mathbf{u}$ is the input to the system. If the disturbance torques are negligible and the spacecraft has no MEDs, then the resulting linearised spacecraft system is expressed by Eq.2.36. The system described using this model is controllable [16].

$$\dot{\mathbf{x}} = A\mathbf{x} + B\mathbf{u} \tag{2.36}$$

where

$$\mathbf{x} = \begin{bmatrix}\boldsymbol{\omega}\\ \mathbf{q}\end{bmatrix} \qquad A = \begin{bmatrix}0_3 & 0_3\\ \frac{1}{2}I_3 & 0_3\end{bmatrix}, \qquad B = \begin{bmatrix}J^{-1}\\ 0_3\end{bmatrix} \tag{2.37}$$

Considering the LQR problem, if matrices Q and R are assumed to be diagonal, as it is often done in engineering design practice and

the inertia tensor J is assumed to be diagonal as well, then the LQR controller has a diagonal structure in its state matrices D and K:

$$\mathbf{u} = -[D, K]\mathbf{x} \tag{2.38}$$

In [16] it is shown, by means of the Lyapunov second method, that if matrices Q and R satisfy one of the two additional constraints, expressed by Eq. 2.39, then the nonlinear system defined by 2.7 and 2.6 is global asymptotically stable.

$$R = cQ_{22} \quad or \quad R = cQ_{22}J \tag{2.39}$$

where c is a constant and Q_{22} is a part of the matrix Q expressed in Eq. 2.40

$$Q = \begin{bmatrix} Q_{11} & 0 \\ 0 & Q_{22} \end{bmatrix} \tag{2.40}$$

3

Spacecraft attitude control

The scope of an attitude control system is to achieve and maintain a nominal attitude. This is done by comparing the information on the current attitude and angular velocity, that is retrieved by the attitude determination system, with the required nominal attitude. Based on this difference a torque is commanded to the actuators. The design of the spacecraft attitude control law depends on the model used to describe the spacecraft dynamics. Depending on the system and mission scenario, the nonlinear model or linearised dynamics can be employed for the control law design. In the case of inertially fixed spacecraft, the linearised system has a simple structure and the use of linear control method is attractive. In [16], for example, is shown that the LQR based on the linearised reduced quaternion model of the inertially fixed spacecraft has an analytical formula. When magnetorquers are used as actuators, only the component of the torque perpendicular to the magnetic field can be actuated. This fact makes the design a challenging task for which different solution have been developed.

In the following sections, different types of control designs will be briefly presented. In Section 3.1 the problem of magnetic attitude control is covered. Some control laws for detumbling and attitude control are presented. In section 3.2 the control of spacecraft equipped

with reaction wheel control is presented. Finally, in section 3.3 the problem of mixed magnetic-mechanical actuation is presented together with the solution described in [19]. The presented approach is then at the basis of the attitude control law described in Chapter 4, where a LTI model is used for the spacecraft.

3.1 Magnetic control

Magnetic control has been used since the beginning of the space era. The first proposal for attitude control using magnetic torques was in the early 1960s [32]. Mainly passive systems were used in the beginning, while the use of active systems become popular later thanks to electronic miniaturisation. In particular, magnetorquers are widely used in small satellites in LEO. They consist of electromagnetic coils with a specified number of turns and area that produce a magnetic dipole interacting with the Earth's magnetic field. For a coil of surface S with normal to the surface $\hat{\mathbf{a}}$, with n turns and with current i the magnetic dipole generated is:

$$\mathbf{m} = niS\hat{\mathbf{a}} \tag{3.1}$$

The generated magnetic dipole interacts with the Earth's geomagnetic field to generate a torque expressed by 2.13, here reported.

$$\boldsymbol{\tau} = \mathbf{m} \times \mathbf{b} \tag{3.2}$$

Magnetic control can be used directly for attitude control or to unload momentum accumulated by reaction wheels. In the latter, the magnetorquers have to counteract only the secular components of the disturbance torques [33]. Other uses are detumbling, initial acquisition, precession control and nutation damping. The use of magnetorquers offers several advantages with the main drawback of the under-actuation around an axis parallel to the external magnetic field and a propensity to control saturation. Indeed, the torque can be only

applied in the plane perpendicular to the external magnetic field, as it is clear from Eq. 3.2. The underactuation is instantaneous because as the spacecraft travels along its orbit, the forbidden direction of actuation becomes available again and, on average, 3 axes control is achieved. This fact has been used to design control laws that contemplate the use of only magnetic actuation.

3.1.1 Detumbling by means of the magnetic actuation

A possible nonlinear control action consists in a magnetic dipole proportional to the cross product between the external magnetic field vector and the angular velocity [34]:

$$\mathbf{m} = \frac{k}{\|\mathbf{b}\|}\boldsymbol{\omega} \times \hat{\mathbf{b}} \tag{3.3}$$

the resultant torque is:

$$\boldsymbol{\tau} = -k(I_3 - \hat{\mathbf{b}}\hat{\mathbf{b}}^T)\boldsymbol{\omega} \tag{3.4}$$

This control torque will send to zero the component of $\boldsymbol{\omega}$ perpendicular to $\mathbf{b}$ but obviously, it won't affect the component parallel to it. If one considers the following Lyapunov candidate function:

$$V = \frac{1}{2}\boldsymbol{\omega}^T J \boldsymbol{\omega} \tag{3.5}$$

and computes $\dot{V}$ using 2.7 and 3.4, than it will find that $\dot{V}$ is only negative defined. Indeed, it is equal to zero not only when $\boldsymbol{\omega} = 0$ but also when $\boldsymbol{\omega}$ is parallel to $\hat{\mathbf{b}}$. This eventuality is avoided if the orbit of the spacecraft is such that the direction of the magnetic field is not inertially fixed [34].

In the case that no angular velocity information is available, [34] proposes a modified version of the well-known B-dot law [35]:

$$\mathbf{m} = -\frac{k}{\|\mathbf{b}\|}\dot{\hat{\mathbf{b}}} \tag{3.6}$$

Using this control law, the angular velocity can be reduced to a value of the same order of magnitude of the orbit rate (about 10^{-3} rad/s).

3.1.2 Magnetic actuation for three-axis attitude control

Magnetic control has been also used to perform a three axis attitude control. In [36] and [37] a feedback control law is proposed for inertial pointing and implemented by the magnetorquers in a projection manner:

$$\mathbf{m} = -k_\omega \mathbf{b} \times \boldsymbol{\omega} - k_q \mathbf{b} \times \mathbf{q} \tag{3.7}$$

where q is vector part of the quaternion. Asymptotic stability is proven provided that certain scaling properties between k_ω and k_q are satisfied.

3.2 MED control

A real spacecraft is not properly a rigid body, either because of the finite stiffness of its components or because it is often equipped with moving parts, for example with Momentum Exchange Devices (MEDs). As the name suggests, these actuators exchange angular momentum with the rest of the spacecraft without changing the overall angular momentum. They do so by spinning a flywheel using an electric motor. Based on their nominal speed they are divided into:

- momentum wheels
- reaction wheels

The momentum wheels have a nominal speed different from zero that provide a gyroscopic stiffness to the spacecraft but make the spacecraft less manoeuvrable. The reaction wheels, on the other hand, have a nominal speed equal to zero. In both cases, the wheels change their speed in response to external torques. The external disturbance torques usually have a periodic component and a secular component. After a certain time, the secular component will bring the wheel to possess an angular momentum beyond which its structural integrity is compromised. For this reason, the wheel needs to be desaturated using other actuators, such as thrusters or magnetorquers. Usually, three reaction wheels are used, with their axis aligned with the spacecraft principal axis or, if redundancy is taken into consideration, more than three reaction wheels are used with different possible configurations. Since these devices don't change the total angular momentum, the torque that they provide is said to be internal (differently from thrusters, for example, that change the total angular momentum by expelling propellant). This fact is reflected in the minus sign in Eq. 3.8. The momentum/reaction wheels can be taken into account with a slight modification of Euler's equations. The total angular momentum can be split into 2 contributions: $J\boldsymbol{\omega}$ is the angular momentum of the spacecraft with the wheels considered at rest with it, $\mathbf{h}$ is the angular momentum of the wheels relative to the spacecraft. If one considers axisymmetric wheels rotating about their axis of symmetry and with the centre of mass lying on it, then the hypothesis of constant tensor of inertia in the body axis holds and the Euler's equations of dynamics are rewritten as:

$$J\dot{\boldsymbol{\omega}} = \boldsymbol{\tau} - \dot{\mathbf{h}} - \boldsymbol{\omega} \times (J\boldsymbol{\omega} + \mathbf{h}) \tag{3.8}$$

The term $-\dot{\mathbf{h}}$ is very important and it can be interpreted as an internal torque. In absence of external torques, the total angular momentum remains constant and this fact is in accordance with the minus sign of the internal torque. If one considers the simple case of

only one wheel, its rotation in one sense causes the rotation of the remaining mass of the spacecraft in the opposite sense. This fact offers a possibility for attitude control of the spacecraft using momentum exchange devices.

Eq. 3.8 describes the dynamics of the spacecraft equipped with one or more MEDs (Momentum Exchange Devices). In the design of the control law, the dynamical model of the motor is also considered. The simplest model is the one of an ideal DC motor in which the torque is linear with the applied voltage; a more realistic model considers also the armature reaction.

3.3 Hybrid magnetic-mechanical attitude control

The performance of a system using magnetorquers as main actuators can be improved by providing it with some sort of mechanical actuation. Thrusters [38] or reaction wheels can be used. For small spacecrafts, MEDs provide longer lifetime and better performance. In [17], the tandem use of reaction wheels and magnetorquers is considered but the two systems are controlled independently. This means that their control torque can overlap and possibly cancel out. In [19] instead, this possibility is avoided by geometrically distributing the required control torque. The required torque is split into two components:

$$\boldsymbol{\tau} = \boldsymbol{\tau}_{\perp} + \boldsymbol{\tau}_{\parallel} \tag{3.9}$$

where $\boldsymbol{\tau}_{\perp} \in Im\{[\mathbf{b}^{\times}]\}$ and $\boldsymbol{\tau}_{\parallel} \in Ker\{[\mathbf{b}^{\times}]\}$. The torque to be provided by the actuation system is calculated as follows:

$$\boldsymbol{\tau}_w = \boldsymbol{\tau}_{\parallel} \qquad \boldsymbol{\tau}_m = \boldsymbol{\tau}_{\perp} \tag{3.10}$$

where $\boldsymbol{\tau}_w$ is the torque to be actuated by the reaction wheels and $\boldsymbol{\tau}_m$ is the one to be actuated by the magnetorquers. The physical interpretation of this control law is straightforward: the magnetorquers are able to provide only torques that lie in the plane perpendicular to the external magnetic field $\mathbf{b}$ and the matrix $[\mathbf{b}^\times]$ maps any vector in the space to its projection in this plane. In other words, the magnetorquers provide the part of the required torque that had a component in the plane perpendicular to the magnetic field. Similarly, the part of the torque parallel to the direction of the magnetic field is provided by the reaction wheels. This law only distributes the required torque that can be calculated using any method. In the case in which less than three reaction wheels are available, the redistribution law is slightly modified. The reaction wheels are able to provide torque in a direction lying in the plane containing their axis (coinciding with the wheel axis if only one wheel is available). This means that only a component of their torque, $\boldsymbol{\tau}_{w\parallel}$, belongs to $Ker\{[\mathbf{b}^\times]\}$ while the other component, $\boldsymbol{\tau}_{w\perp}$, needs to be compensated by the magnetorquers. In this case, control overlap cannot be always avoided and there is an underactuation whenever the external magnetic field is perpendicular to the plane generated by the wheel axis direction. When only one reaction wheel is used, the torques to be actuated by the wheel and the magnetorquers are evaluated as follows:

$$\boldsymbol{\tau}_w = \frac{\mathbf{b}^T\boldsymbol{\tau}}{b_3} I_3 \qquad \boldsymbol{\tau}_m = [\hat{\mathbf{b}}^\times]^T[\hat{\mathbf{b}}^\times](-\boldsymbol{\tau}_w + \boldsymbol{\tau}) \tag{3.11}$$

In this case, the wheel axis is chosen to coincide with the third axis but it could have been the first as well as the second. The control torque commanded to the wheel can be directly actuated, while the control that can be actuated by the magnetorquers has to satisfy Eq.

$$\boldsymbol{\tau}_m = \mathbf{m} \times \mathbf{b} = [\mathbf{b}^\times]^T\mathbf{m} \tag{3.12}$$

This equation cannot be solved directly for $\mathbf{m}$, since $[\mathbf{b}^\times]^T$ is not

invertible. In [19] the magnetic dipole is chosen in such a way to minimize the cost function 3.13 with respect of m_3, yielding to 3.14.

$$\mathcal{J}_m(m_3) = \frac{1}{2}\mathbf{m}^T\mathbf{m} = \frac{1}{2}\left(m_1^2 + m_2^2 + m_3^2\right) \tag{3.13}$$

$$\mathbf{m} = \begin{bmatrix} \frac{1}{b_3}\left(-\tau_{m2} + m_3 b_1\right) \\ \frac{1}{b_3}\left(\tau_{m1} + m_3 b_2\right) \\ \frac{1}{\mathbf{b}^T\mathbf{b}}\left(\tau_{m2} b_1 - \tau_{m,1} b_2\right) \end{bmatrix}, \quad \forall b_3 \neq 0 \Leftrightarrow \mathbf{m} = \frac{[\mathbf{b}^\times]\boldsymbol{\tau}_m}{\mathbf{b}^T\mathbf{b}} \tag{3.14}$$

From Eq. 3.12 is clear that the underactuation happens when the wheel axis is perpendicular to the magnetic field direction. In [19] is argued that this kind of underactuation is only instantaneous, since all directions become available as the spacecraft travels along its orbit, not that dissimilar from what happens when using only magnetorquers.

4

Attitude control design and simulations

The geometric decomposition of the control torque, described in 3.3, can be used in conjunction with any control scheme. In [19] an adaptive control scheme is used, while in [28] a Linear Time Variant (LTV) input strictly passive controller is used as wheel as in [39]. To the best of this author's knowledge, there were no examples of this strategy being applied in conjunction with a LTI controller. This simple yet effective approach for control law design is used here by implementing a slightly modified version of the geometric approach.

In Section 4.1, the design attitude control scheme used in this work is described. In Section 4.2, the performances of the control law is tested for different orbit inclinations and wheel designs through numerical simulations. Finally, in Section 4.3, the stability of the non-linear system with respect to parameters variations is studied by means of Monte-Carlo approach.

4.1 Control formulation

The distribution law described in [19] is modified to allow for an additional degree of freedom on the control torque commanded to the wheel. The new control distribution law is shown in Eq, 4.1, where it

is assumed that the wheel is mounted on the third axis. The desired dipole is then calculated using Eq. 3.14.

$$\boldsymbol{\tau}_w = k_{wh}\frac{\mathbf{b}^T\boldsymbol{\tau}}{b_3}I_3 \qquad \boldsymbol{\tau}_m = [\hat{\mathbf{b}}^\times]^T[\hat{\mathbf{b}}^\times](-\boldsymbol{\tau}_w + \boldsymbol{\tau}) \tag{4.1}$$

The required torque is calculated as a state feedback (see Eq. 2.7.5) using a LQR based on the LTI model of an inertial pointing spacecraft (2.37). The cost index weight Q is constructed in the following way:

$$Q = \begin{bmatrix} Q_{11} & 0 \\ 0 & Q_{22} \end{bmatrix} = \begin{bmatrix} Q_w & 0 \\ 0 & Q_q \end{bmatrix} \tag{4.2}$$

4.2 Orbit inclination and wheel design selection

The designed attitude control law was tested in *Simulink®* in the case of three magnetorquers and one reaction wheel. As stated above, the system is underactuated whenever the axis of the reaction wheel is perpendicular to Earth's magnetic field vector. This means that the performance of the system depends on the inclination of the orbit and on the axis on which the wheel is mounted. The design of such system is thus constrained by this condition to a certain set of orbit inclination and wheel positioning. In order to characterise the system's behaviour to changes in these conditions, 12 simulations were performed. The orbit inclination was varied in the set $(0°, 30°, 60°, 90°)$ while the wheel axis was aligned with one of the three axes of the spacecraft at the time. The spacecraft characteristics are resumed in Table 4.1. They have been chosen considering a 3U CubeSat mission in Low Earth Orbit. The disturbance torques described in Section 2.5 has been also included in the model while measurement errors were not considered at this stage of the design. The modelled environmental torques are the gravity gradient torque, the aerodynamic torque, the solar radiation pressure torque and the residual dipole torque. The maximum values for the

disturbance torques and the actuators characteristics are resumed in Table 4.2.

Parameter	Symbol	Value	Units
	Spacecraft data		
Principal moments of inertia	J_{11},J_{22},J_{33}	0.0283, 0.0323, 0.0127	Kgm^2
	Orbit data		
Semi-major axis	a	6771	Km
Eccentricity	e	0	
Period	T	5545	s
	Initial conditions		
Angular velocity	$\boldsymbol{\omega}_0$	-0.0063, -0.0026, 0.0025	rad/s
Euler angles	ψ_0,θ_0,ϕ_0	9, 5, 8	deg
Magnetic field maximum norm	$\|\mathbf{b}\|_{max}$	3.7×10^{-5}	T

Table 4.1: Spacecraft and orbit data, with initial condition

The weight matrices for the LQR formulation were $Q_w = I_3$ and $Q_q = 0.1I_3$, where I_3 is the 3x3 identity matrix. The weight matrix R and the wheel k_w were the result of a tuning and were set equal to $10I_3$ and 0.1 respectively. The resulting gain matrix D and K (see Eq. 2.7.5) are:

$$D = \begin{bmatrix} 0.3176 & 0 & 0 \\ 0 & 0.3178 & 0 \\ 0 & 0 & 0.3169 \end{bmatrix} \quad K = \begin{bmatrix} 0.0316 & 0 & 0 \\ 0 & 0.0316 & 0 \\ 0 & 0 & 0.0316 \end{bmatrix} \tag{4.3}$$

The results of the simulations showed that the ACS is able to stabilise the system in most combinations of orbit inclination and wheel design. The unique exception was found to be an orbit inclination of 90° and the wheel aligned with the second axis. In that case, indeed, the direction of the Earth's magnetic field vector is almost perpendicular to the wheel axis (see Fig. 4.1 (b)). This means that the wheel is not effective in providing the torque in the direction parallel to the

Parameter	Symbol	Value	Units
Disturbance torques			
Gravity gradient torque	$\tau_{gg,max}$	3.5×10^{-8}	Nm
Aerodynamic torque	$\tau_{a,max}$	4.5×10^{-7}	Nm
Solar radiation pressure torque	$\tau_{srp,max}$	7.3×10^{-9}	Nm
Residual dipole value	$\mathbf{m}_{res}$	0.5	Am^2
Residual dipole torque	$\tau_{m,res}$	1.9×10^{-5}	Nm
Actuators			
Wheel moment of inertia	J_w	2.11×10^{-6}	$Kg\ m^2$
Maximum wheel torque	$\boldsymbol{\tau}_{w_{max}}$	2.3×10^{-4}	Nm
Maximum magnetic dipole	$\mathbf{m}_{max}$	1	Am^2
Maximum magnetorquers torque	$\tau_{m,max}$	3.7×10^{-5}	Nm

Table 4.2: Maximum disturbance torques and actuators characteristics

magnetic field, which is also the direction of underactuation for the magnetorquers. The results in terms of steady error of Yaw, Pitch and Roll, are shown in Table 4.3

		Wheel axis		
		1	2	3
i	0°	[0.012 0.048 0.041]	[0.012 0.060 0.041]	[0.012 0.048 0.041]
	30°	[0.007 0.045 0.041]	[0.007 0.046 0.040]	[0.007 0.045 0.040]
	60°	[0.008 0.038 0.034]	[0.008 0.038 0.034]	[0.008 0.038 0.034]
	90°	[0.015 0.035 0.028]	[0.938 1.943 75.741]	[0.015 0.035 0.028]

Table 4.3: Steady-state error of [Yaw Pitch Roll] for different orbit inclination and wheel axis alignment

Looking at the effort required by the actuators, the best configuration found is an orbit inclination of 0° (equatorial orbit) and the wheel aligned with the third axis. Indeed, in that case, the direction of the Earth's magnetic field is almost parallel to the wheel's axis (see Fig. 4.1 (a)) and the control torque required by the wheel, expressed by Eq. 4.1, is minimum. The results for this case in terms of Euler angles are shown in Fig. 4.2. For all the other orbit inclinations and wheel alignment, the control torque required by the wheel increases to

high values whenever the wheel axis is perpendicular to the Earth's magnetic field, as shown in Fig. 4.3, in which the wheel is aligned with the third spacecraft body axis. Since the torque required by the magnetorquers depends also on the wheel torque via Eq. 4.1, the peaks on the wheel torque result also in peaks in the commanded dipoles. Motivated by these results, it has been chosen to use an equatorial orbit and to have the wheel's axis aligned with the spacecraft third axis. It is worth noting that an equatorial orbit is the worst case for a spacecraft equipped with only magnetorquers since the magnetic field has an almost constant direction.

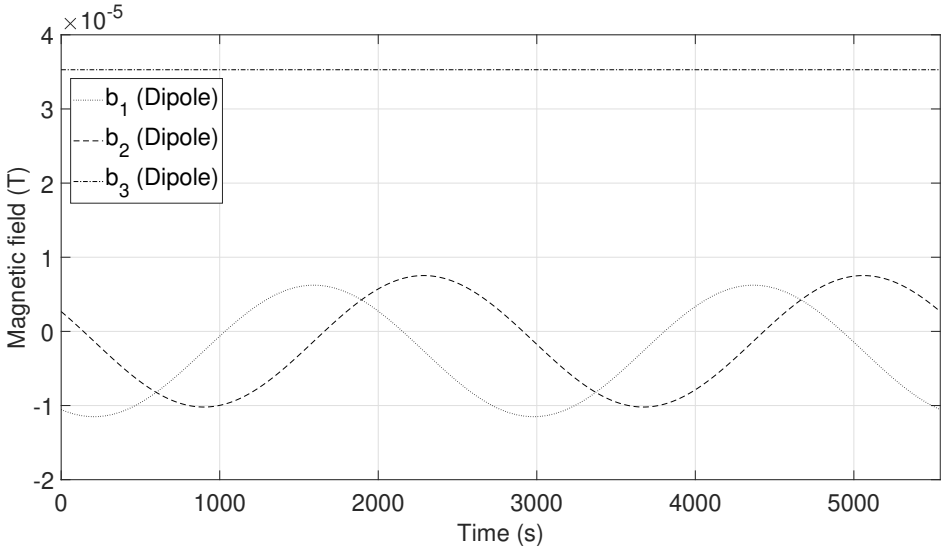

(a)

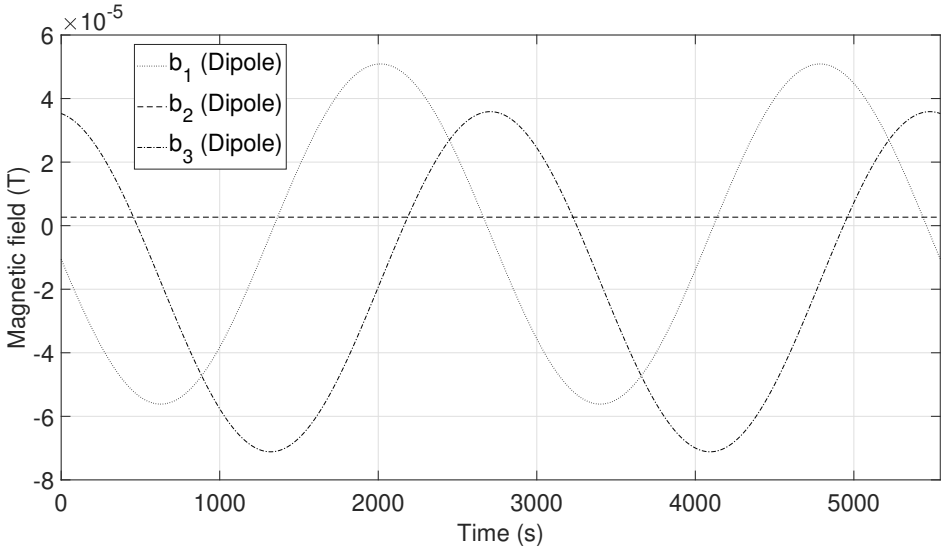

(b)

Figure 4.1: Magnetic field components in ECI coordinates system using the dipole approximation, 0° orbit inclination (a) and 90° orbit inclination (b).

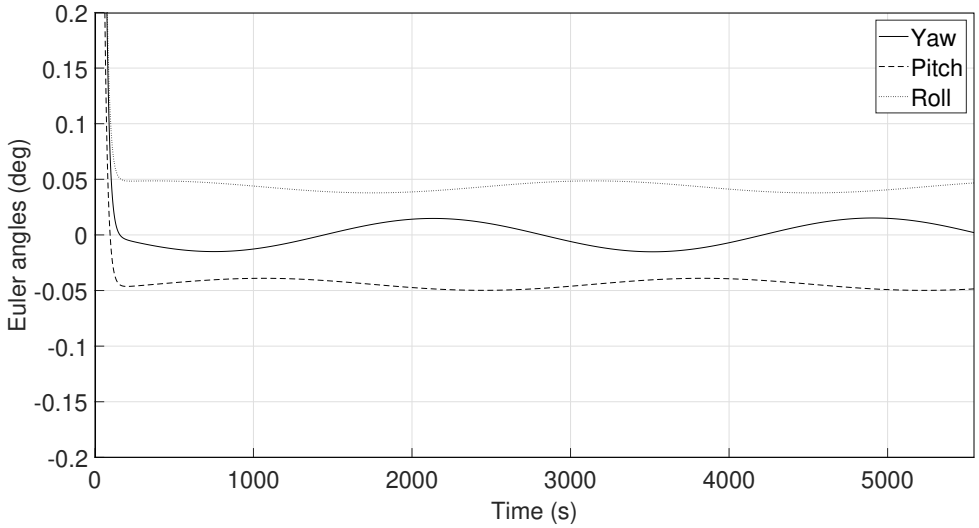

Figure 4.2: Euler angels for a wheel on the third axis, orbit inclination = 0 deg

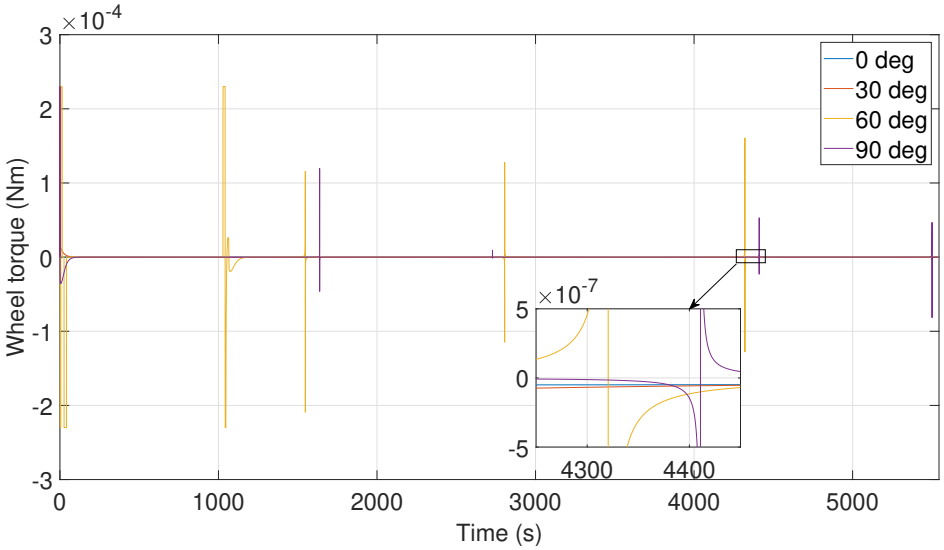

Figure 4.3: Wheel torque at different orbit inclination in the case the wheel is mounted on the third spacecraft body axis

4.3 Monte Carlo tests

Effects of environmental torques parameters variation on the ACS performance were studied by means of Monte Carlo approach. For a specified span of possible parameters, initial conditions and the off-diagonal term of the inertia matrix 300 Monte Carlo simulations were set. The attitude sensors and the gyroscopes were modelled accordingly to the expected performances of a typical attitude determination system on a 3U CubeSat. State of the art systems can reach an attitude determination accuracy in the order of 0.1° [40] in case no star tracker is employed, which is not expected to be available for the considered Attitude Determination and Control System class. Fig. 4.4 shows the effect of the measurements error on the pointing accuracy of a spacecraft. The LQR weight matrices are $Q_w = I_3$ and $Q_q = 0.01 I_3$, $R = 1 \times 10^3 I_3$ and the wheel gain is $k_w = 0.05$. The resulting gain matrix D and K are reported in Eq. 4.4 while the other Monte Carlo simulations settings are resumed in Table 4.4.

$$D = \begin{bmatrix} 0.0330 & 0 & 0 \\ 0 & 0.0332 & 0 \\ 0 & 0 & 0.0322 \end{bmatrix} \quad K = \begin{bmatrix} 0.0032 & 0 & 0 \\ 0 & 0.0032 & 0 \\ 0 & 0 & 0.0032 \end{bmatrix} \tag{4.4}$$

Parameter	Set of values	Units
Off-diagonal terms inertia matrix	$[0.1, 1] \times 10^{-3}$	$Kg\ m^2$
Atmospheric density	$[0.05, 5] \times 10^{-12}$	Kg/m^3
Residual dipole	Intensity 0.5 and random direction	$A\ m^2$
Initial angular velocity	$[0.057, 0.57]$	deg/s
Initial Euler angles	$[0, 180]$	deg

Table 4.4: Monte Carlo simulations setting

The magnetic torque due to the residual dipole was the main torque acting on the spacecraft, with an order of magnitude of 10^{-5}

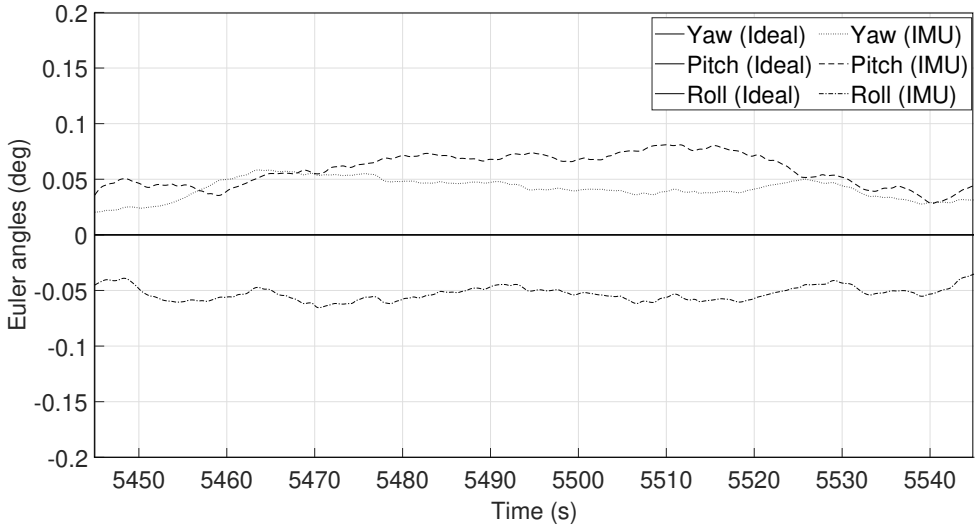

Figure 4.4: Attitude error in the case measurement errors are absent (Ideal) and in the case they are present (IMU)

Nm, followed by the aerodynamic torque, whose magnitude depends on the atmospheric density, and then by the others environmental torques. The results of the simulations, in terms of *steady-state error*, are reported in Fig. 4.5 while Fig. 4.6 shows the evolution with respect of time of the Euler angles for the first 500 seconds of the simulations.

	Yaw	Pitch	Roll
Mean value	$0,14°$	$0,41°$	$0,41°$
Standard deviation	$0,10°$	$0,29°$	$0,26°$

Table 4.5: Mean value and standard deviation of Euler angles' steady state values

For the 97% of the simulations, the settling time is under 280 sec while 3% of the simulations reported anomalous results in which the settling time is comparable with the orbital period. As expected, the best pointing accuracy is reached on the third axis thanks to the presence of the reaction wheel. Table 4.5 reports the mean value and the standard deviation of the steady-state value of the Euler angles. The results show that the designed control system is capable of ensuring good pointing accuracy also in presence of disturbances and parameters

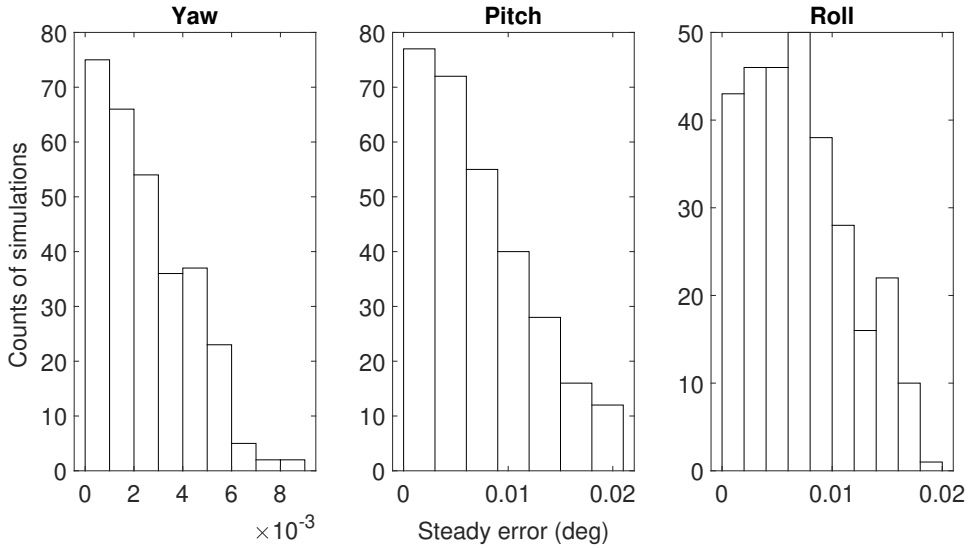

Figure 4.5: Results of Monte Carlo simulations in terms of steady-state error, Euler angles

variations. It's important to remark that the pointing accuracy and the stability of the control system are dependent on the orbit inclination and the wheel design. Indeed, the system is underactuated whenever the reaction wheel is parallel to the external magnetic field.

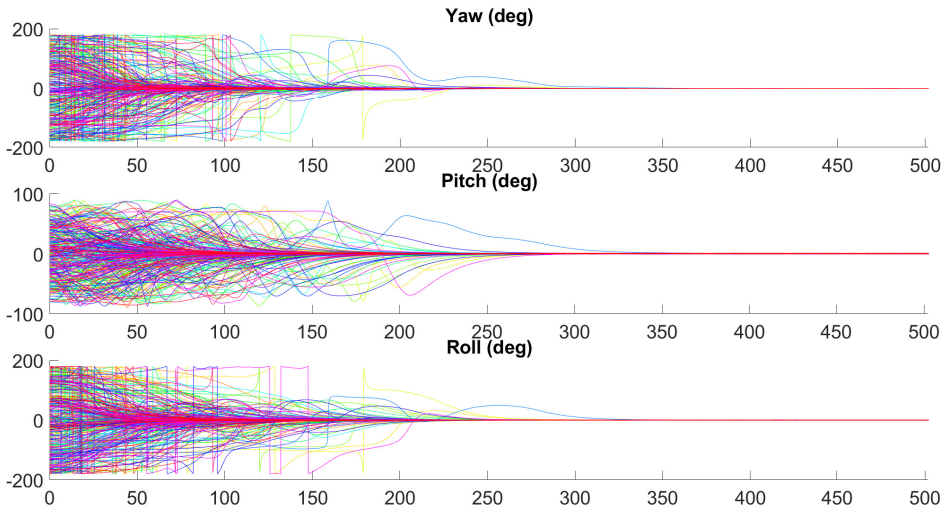

Figure 4.6: Time evolution of the Euler angles for the first 500 seconds of simulation

5

Mass balancing overview and experimental testing

To make possible attitude control experiments, the control torque have to be larger than the disturbance one. As pointed out in Chapter 2, the disturbance torque due to the unbalance is the biggest one affecting the simulator. The gravity torque depends on the distance between CM of the structure and CR. The former can be moved in space and brought to coincide with the latter through some balancing procedure. Even when this is done, any change in the layout of the components in the structure, also a movement of a cable, could shift the CM to a new position that in general will differ from the one of the CR. This fact requires the balancing procedure to be fast, accurate and repeatable. This is obtained for the Attitude Simulator Testbed using the ABS. The ABS relies on three stepper motors driving three $0.041Kg$ masses. The Automatic Balancing System is able to move the CM in a limited region of the three-dimensional space that of course included the CR location. For points outside of this region, manual balancing has to be performed. This is the case, for instance, when the structure is first assembled.

5.1 Manual balancing

The manual balancing procedure is performed by properly placing the components on the plate and through the adjustment of 4 bolts (visible in Fig. 2.5) linking the plate to the rotating hemisphere of the air bearing. The bolts can be adjusted both in height, through their screwing, and in the plane, thanks to the presence of 2 slots. The manual balancing procedure is concluded when the CM is moved inside the reachable workspace of the ABS. This is effective only in balancing the offset in the direction perpendicular to the gravity field, while the parallel component is more difficult to be compensated. The torque that can be generated by the balancing masses is indeed physically confined in the direction perpendicular to the gravity field [27], [9]. For this reason, it is convenient to split the balancing procedure into two or more consequent operations, separating the in-plane balancing from the balancing in the vertical direction.

5.2 Automatic balancing

In [9], a two-step iterative balancing procedure is proposed. Inertia estimation is followed by balancing on the x-y plane and by estimation of the unbalance vector in the z direction through sampling of free oscillation, and finally by the balancing in the z direction. The two last steps are repeated until no further reduction of the unbalance vector component in the z direction is observed. In here, the inertia tensor is indeed assumed to be known and constant through the balancing procedure. Even if this is not strictly true, the procedure still allows to reach a satisfactory level of residual torque. In particular, the used procedure consists of four steps, three of which are iterative:

1. inertia estimation

2. in-plane balancing

3. residual torque estimation

4. balancing in the vertical direction

The first step, described in 5.2.1, consists in the inertia estimation and it is performed only once. This is done through sampling of free oscillation, as described later. The full matrix of inertia estimation is in turn preceded by the estimation of the inertia properties around the z axis. This information is gathered using the precise knowledge of the wheel inertia and the processing of angular velocity data. Following the inertia estimation, three iterative steps are performed. The first of these, described in 5.2.2, consists in a PID control algorithm that is used to control the two shifting masses on the x-y plane. Once the in-plane component of the unbalance vector is compensated, the next step consists of the estimation of the residual torque. This information, together with the one on the type of pendulum, is then used to compensate for the vertical component of the unbalance vector.

The residual torque estimation and the compensation of the unbalance vector in the z direction, are described in 5.2.3. The last three steps are iterated until no further improvement in the residual torque is observed.

5.2.1 Inertia characterization

The estimation of the residual torque requires the knowledge of the inertia parameters of the moving part of the platform, expressed by

$$J = \begin{bmatrix} J_{xx} & J_{xy} & J_{xz} \\ J_{xy} & J_{yy} & J_{yz} \\ J_{xz} & J_{yz} & J_{zz} \end{bmatrix} \tag{5.1}$$

The information on the inertia properties of the wheel together with the one on the angular velocity data gathered by the IMU, are used to estimate the J_{zz} component of the inertia matrix. This information is then used to increase the accuracy of the inertia matrix estimation

process. In this process, the balancing mass in the z direction is brought at its lower limit value. This allows having a strong gravity torque that maintains the platform in the horizontal plane while minimising the angular velocity components in the x and y directions. Using the assumption of angular velocity parallel to the z axis, assuming the axis of the wheel is perfectly aligned with this axis and that the external torques acting on the system are much smaller than the one provided by the torque, Eq. 3.8 simplifies in:

$$J_z \omega_z = -\dot{h} \tag{5.2}$$

The equations describing the dynamics of the wheel is:

$$g = J_w(\dot{\Omega}_w + \dot{\omega}_z) = \dot{h} + J_w \dot{\omega}_z \tag{5.3}$$

where g is the torque applied to the wheel, J_w is the wheel moment of inertia component on the rotation axis and $\dot{\Omega}_z$ is the angular acceleration around the same axis. Eq. 5.2 and 5.3 can be combined to give Eq. 5.4 that can be solved for J_z once the other variables are known.

$$(J_z - J_w)\dot{\omega}_z = -g \tag{5.4}$$

The remaining components of the platform tensor of inertia are estimated through sampling of free oscillations and numerical differentiation of filtered angular velocity data. The estimation process is based on [9] and relies on the partial knowledge of the unbalance vector and of the inertia parameter, namely J_{zz}. Indeed, a known unbalance is imposed in the x-y plane after the in-plane balancing process is performed. These values are then used to estimate the residual torque during the automatic balancing process.

5.2.2 In plane balancing using shifting masses

The control law used for the in-plane-balancing is based on the PID controller described in [9], here reported for completeness. As a first

step, the equations of dynamics are rewritten assuming a rigid body equipped with linearly moving masses. The CR, rather than the CM, is used as the origin of the body reference system $\mathcal{F}$, since the former is inertially fixed. The axis of this reference system is coincident with the one of the IMU. The inertial reference frame has its origin in the CR and has the z axis aligned with the local vertical. The equation expressing the gravity vector $\mathbf{g}$ in the body frame is:

$$\mathbf{g}_b = A_b^i \mathbf{g}_i \tag{5.5}$$

where A_b^i is the DCM expressing the rotation between the body fixed frame and the inertial frame. Called $\mathbf{r}_{CM}$ the position vector of the CM in the body frame, the torque produced by the offset between the CR and CM is:

$$\boldsymbol{\tau}_{CM} = m_{tot}\mathbf{g}_b \times \mathbf{r}_{CM} \tag{5.6}$$

where m_{tot} is the mass of the free-to-rotate body. The torque created by the balancing system is equal to:

$$\boldsymbol{\tau}_b = m_{tot,b}\mathbf{g}_b \times \mathbf{r}_b \tag{5.7}$$

where $m_{tot,sm}$ is the sum of the mass of the shifting masses and $\mathbf{r}_b$ is set to provide $\tau_{CM} = \tau_b$. It can be shown that the effect of three sliding masses is the same as having a single mass displaced of a quantity equal to the sum of the displacement of the masses [27]. Defining the inertia matrix J as the sum of the inertia matrix of the platform without the shifting masses plus the contribution of the shifting masses and neglecting their contribution to the angular momentum variation (it can be done since the low speed of the stepper motors), the Euler equation of dynamics 2.7 becomes [9]:

$$J\dot{\boldsymbol{\omega}} = \boldsymbol{\tau}_{CM} + \boldsymbol{\tau}_b - \boldsymbol{\omega} \times (J\boldsymbol{\omega}) \tag{5.8}$$

that in case of diagonal inertia matrix $J = diag(J_x, J_y, J_z)$ become

$$\begin{aligned} J_x\dot{\omega}_x + (J_z - J_y)\omega_y\omega_z &= m_tot(r_{CM,z}g_y - r_{CM,y}g_z) + \tau_{b,x} \\ J_y\dot{\omega}_y + (J_x - J_z)\omega_x\omega_z &= m_tot(r_{CM,x}g_z - r_{CM,z}g_x) + \tau_{b,y} \\ J_z\dot{\omega}_z + (J_y - J_x)\omega_x\omega_y &= m_tot(r_{CM,y}g_x - r_{CM,x}g_y) + \tau_{b,z} \end{aligned} \tag{5.9}$$

Only the first two equations can be considered since $\tau_{b,z}$ is null in the target position. Introducing the Euler angles roll ϕ, pitch θ and yaw γ and assuming small angles and rate, Eq. 5.9 can be linearised, resulting in:

$$\begin{aligned} J_x\ddot{\phi} &= m_tot(r_{CM,z}g_y - r_{CM,y}g_z) + \tau_{b,x} \\ J_y\ddot{\theta} &= m_tot(r_{CM,x}g_z - r_{CM,z}g_x) + \tau_{b,y} \end{aligned} \tag{5.10}$$

$\tau_{b,x}$ and $\tau_{b,y}$ are calculated as Proportional Integral feedback of ϕ and θ respectively plus a term proportional to the in-plane component of the angular velocity.

$$\tau_{b,x} = -k_p\phi - k_i\int_0^t \phi dt + k_\omega\omega_x \tag{5.11}$$

$$\tau_{b,y} = -k_p\theta - k_i\int_0^t \theta dt - k_\omega\omega_y \tag{5.12}$$

The position for the balancing masses are then calculated assuming that at the equilibrium $g_x = 0$ and $g_y = 0$ [9]:

$$r_x = \frac{\tau_{b,y}}{m_{tot}g_z} \tag{5.13}$$

$$r_y = \frac{\tau_{b,x}}{m_{tot}g_z} \tag{5.14}$$

In the practical implementation, the tilt angles are calculated using the gravitational acceleration:

$$\phi = \frac{g_y}{\|g\|} \qquad \theta = \frac{g_x}{\|g\|} \tag{5.15}$$

as it provides better accuracy under almost-static conditions [9].

5.2.3 Residual torque estimation and compensation in z direction

Once the in-plane balancing process is completed, the residual torque caused by the vertical unbalance can be estimated. For small angular speed, the torque caused by the offset between CR and CM can be considered the main disturbance torque acting on the platform [9]. Its value can be estimated by inspecting the time variation of the angular momentum, described by Eq.5.16:

$$\dot{\mathbf{L}} = J\dot{\boldsymbol{\omega}} = \boldsymbol{\tau}_{MC} - \boldsymbol{\omega} \times (J\boldsymbol{\omega}) \tag{5.16}$$

Eq. 5.16 requires the knowledge of the angular acceleration $\dot{\boldsymbol{\omega}}$. This information, not directly provided by the IMU, is retrieved through differentiation of the angular velocity, performed using Savitzky-Golay filtering. The angular velocity data are collected via sampling of free-oscillation, with sampling frequency equal to 20Hz. A free-oscillation motion is obtained either by manually tilting the platform at its maximum tilt angle and then realising it or by manually placing it in a horizontal position and then releasing it. The reason for having two procedures is that the air-bearing platform, with an unbalance in the z direction, behaves like a rigid 3D pendulum. The 3D pendulum has two equilibrium points: *hanging equilibrium* when the CM is below the CR and *inverted equilibrium* when the CM is above the CR [41]. Only the hanging equilibrium is a stable equilibrium point while the inverted equilibrium is unstable. When the platform exhibited a pendulum-like behaviour the first procedure is used while the second procedure is used in the case of an inverted pendulum. In both cases, the angular velocity measurements can be used for the residual torque estimation. Based on

the type of pendulum-like behaviour, the vertical mass is then moved either in the upward direction (in case the CM is below the CR) or in the downward direction (CM above CR). After some iterations of the procedure, the offset in the z direction becomes comparable with the residual unbalance in the x-y plane, and the type of pendulum cannot be easily identified. In that case, only the residual torque information is used to determine the direction towards which moving the vertical balancing mass, in a try-and-error process. The in-plane balancing and the residual torque estimation together with the vertical balancing are repeated until the residual torque does not further reduce.

5.2.4 Experimental results

Inertia estimation

The wheel moment of inertia has been obtained using its CAD model and is equal to $8171.43 \times 10^{-9} Kgm^2$. The tests aiming to estimate J_{zz} are performed by commanding a known torque to the wheel and by collecting the platform angular velocity data provided by the IMU. A Savitzky-Golay filter is used to process the angular velocity data that is then numerically differentiated to obtain the angular acceleration information. Finally, Eq. 5.4 is used to calculate J_{zz}. The process is repeated with different values of wheel torque in order to obtain statistical significance. The result of one of these experiments is shown in Fig. 5.1, where a torque of $0.0003Nm$ was commanded to the wheel. The J_{zz} value is estimated to be $6.45 \times 10^{-3} Kgm^2$. The remaining components of the platform tensor of inertia are then estimated. Fig. 5.2 shows the estimated value for J_{xx} and J_{yy} in the case an imposed unbalance in the x direction caused by a distance between CR and CM of $6mm$. Several tests were performed and the estimated matrix of inertia is:

$$J = \begin{bmatrix} 0.0092 & 0 & 0.0010 \\ 0 & 0.0099 & 0 \\ 0.0010 & 0 & 0.0064 \end{bmatrix} \tag{5.17}$$

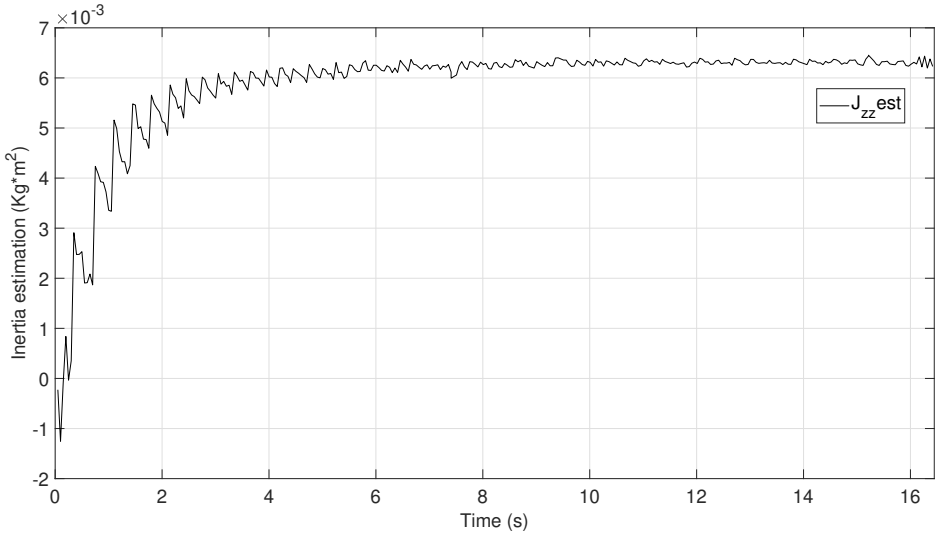

Figure 5.1: J_z inertia estimation in the case the wheel provides $0.0003Nm$ torque

Mass balancing

In Fig. 5.3 the position of the two balancing masses for one procedure is shown. The gains used in this case are reported in Table 5.1. The position commanded to the masses is characterized by random noise, caused mainly by the gyroscope data and by the vibrations induced by the dynamics of the moving masses themselves. To reduce vibrations, in 5.3 the angular velocity damping is performed by the magnetorquers.

k_p	k_i	k_ω
0.0005	0.000005	0.0025

Table 5.1: Gain used for in-plane balancing

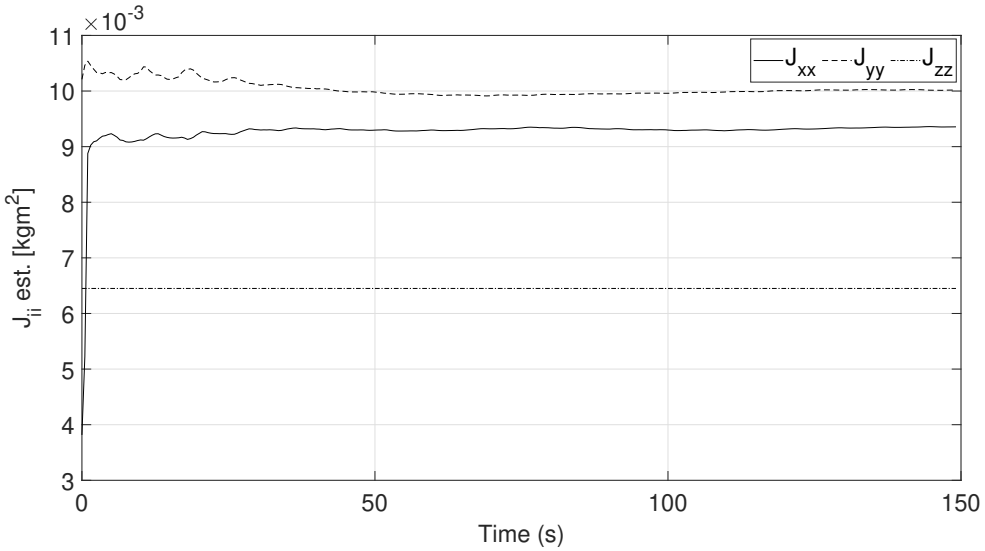

Figure 5.2: Inertia estimation in the case of a distance between CM and CR of $6mm$ in the x direction (only J_{xx} and J_{yy} are shown).

As a result of the balancing process, the gravity torque acting on the platform is reduced to values in the order of $10^{-4}Nm$. Fig. 5.4 shows an example of the estimation of the residual torque. These values are greater than the one reported in [10], probably because of the simplified balancing procedure used here. For this reason, it was decided to enhance the control authority of the magnetorquers by increasing the magnitude of the magnetic field generated by the HC, as described in 6.1.

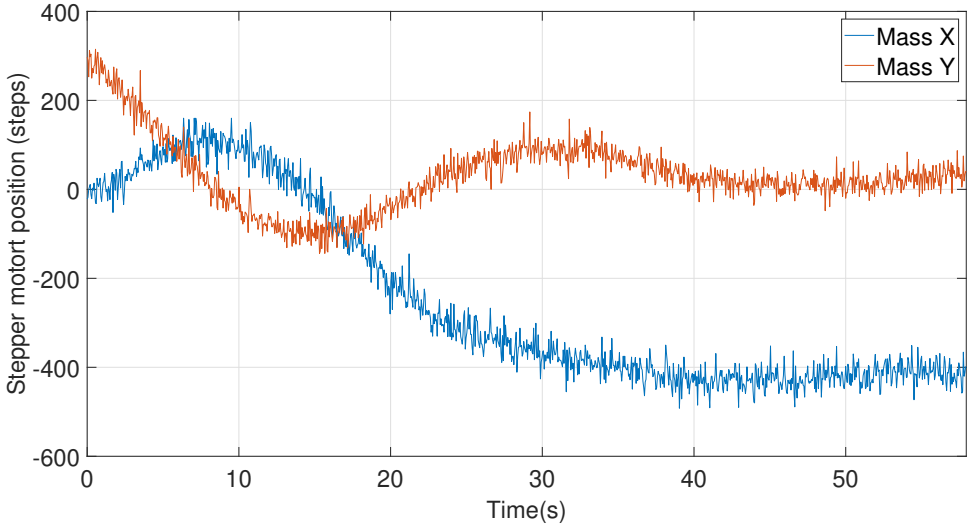

Figure 5.3: Shifting masses position

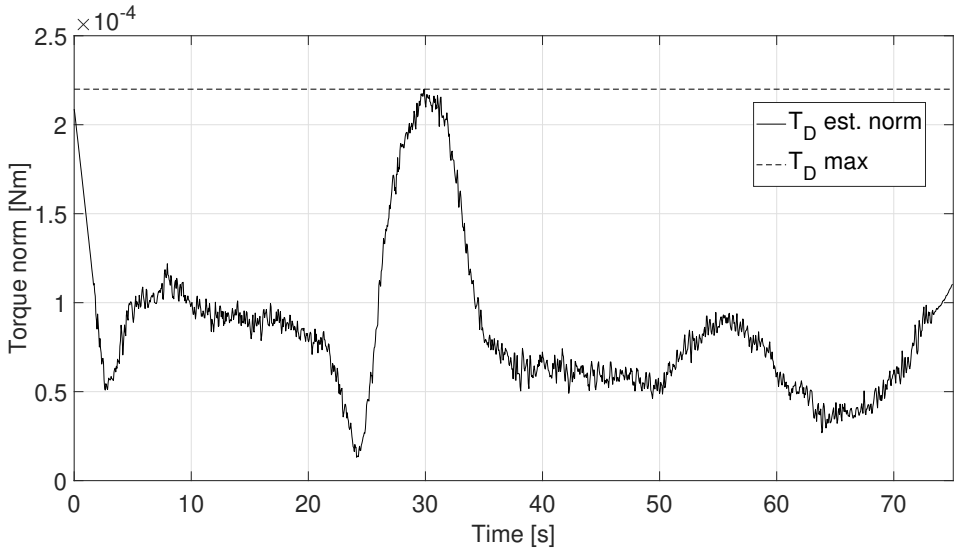

Figure 5.4: Estimation of the residual torque after the balancing procedure

5.3 Automatic mass balancing using moving masses and magnetorquers

The performance of the automatic balancing system are limited by the performance of the IMU. As noted earlier, the noise present on the gyroscope data reflects in a commanded position for the stepper motors that is noisy as well (see Fig. 5.3) and that can produce unwanted mechanical vibrations. The magnetorquers, on the other hand, are characterised by the absence of mechanical parts in relative movement and offer smoothness of actuation. For this reason, the use of the automatic in-plane mass balancing system together with magnetorquers has been investigated. The control for the ABS is still formulated using Eq. 5.11 but with $k_\omega = 0$. The angular velocity damping is provided by the magnetorquers, where the control torque is calculated using Eq. 6.5 and the dipole using Eq. 6.6. Fig. 5.5 compares the angular velocity data from the gyroscopes in the case of the mass balancing procedure described in 5.2.2 (a) is used and the approach described here is used instead (b). The gain used are reported in Tab 5.2. The stepper motor positions in the case of hybrid balancing are shown in Fig. 5.6. Both gyroscope and stepper motor position data show that the new method is effective in reducing mechanical vibrations. Finally, in Fig. 5.7 the estimation of the residual torque, after that the modified balancing process has been performed, is reported.

Actuators	k_p	k_i	k_ω
Only motors	0.0005	5×10^{-6}	0.0025
Motors and magnetorquers	0.001	5×10^{-6}	20

Table 5.2: Gain used for in-plane balancing in the case only stepper motors are used and in the case they are used with magnetorquers

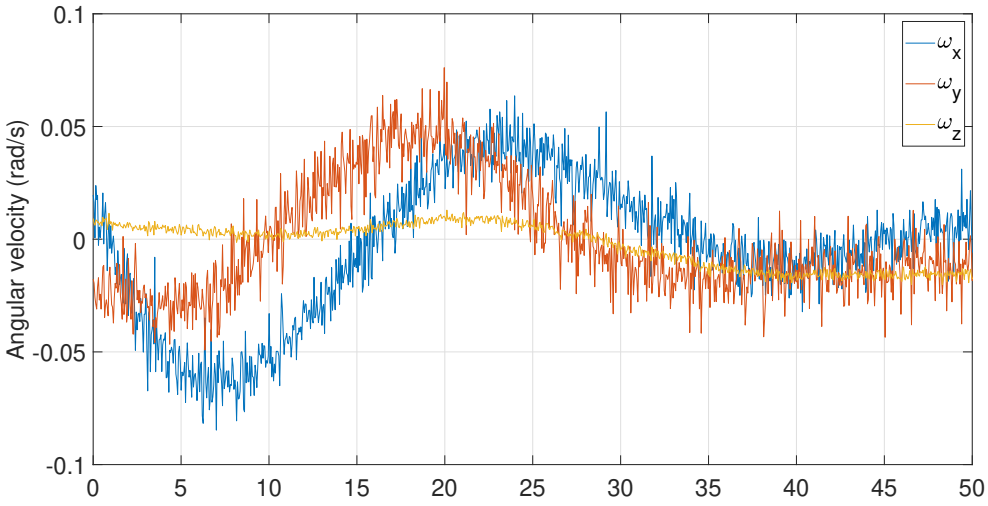

(a)

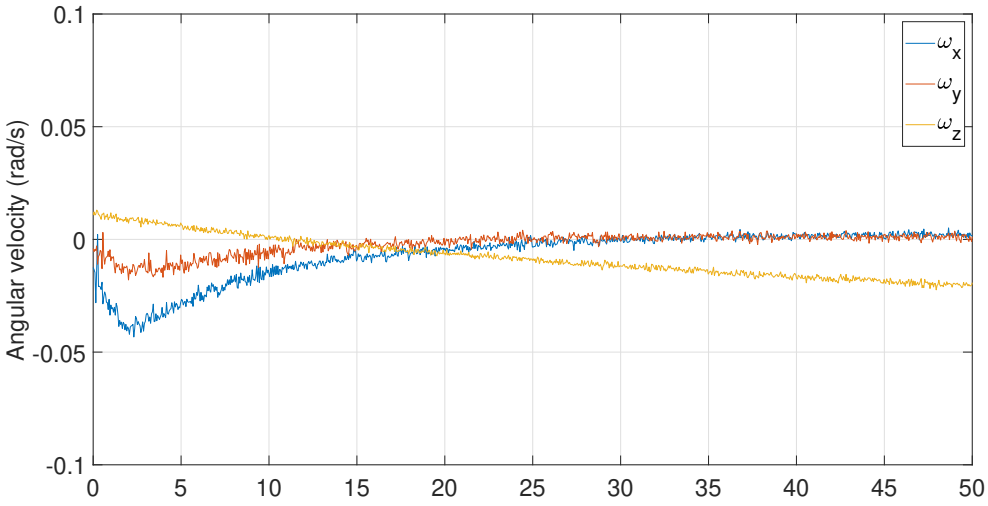

(b)

Figure 5.5: Gyroscope data in the case the angular velocity damping is provided by the stepper motors (a) and in the case it is provided by the magnetorquers (b)

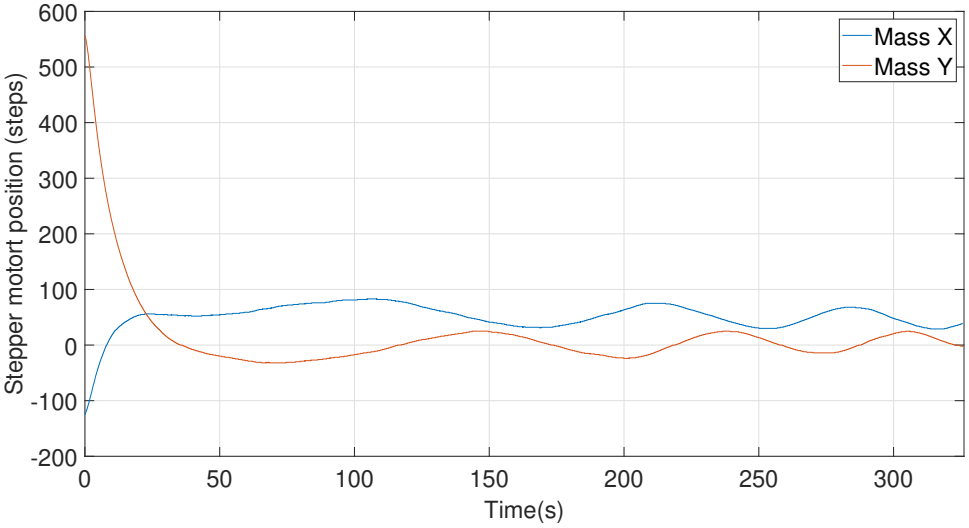

Figure 5.6: Stepper motor position in the case of hybrid balancing

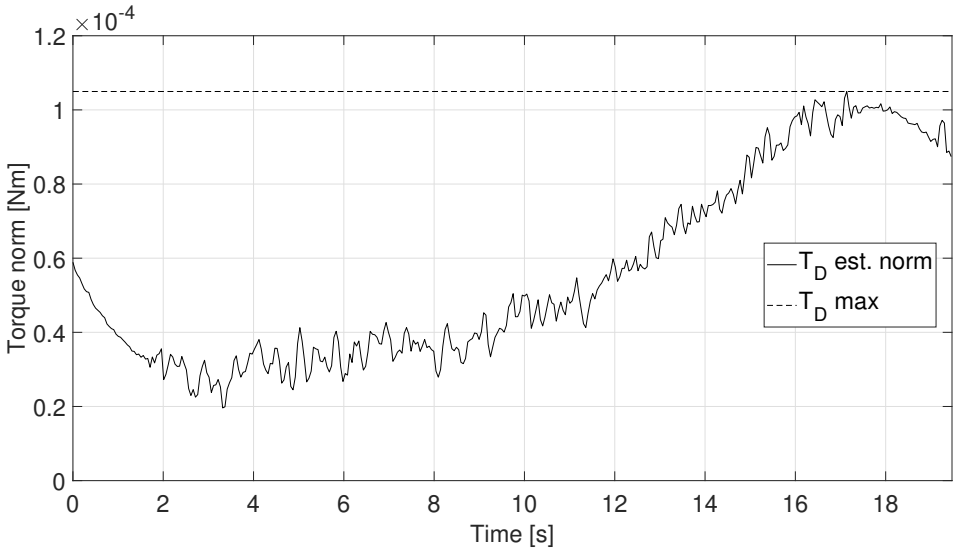

Figure 5.7: Estimation of the residual torque after the modified balancing procedure

6

Mixed magnetic/mechanical control experimental testing

The last part of the thesis work has been dedicated to the experimental test of the mixed magnetic/mechanical ACS on the AST of the University of Bologna. This included both the test of the magnetorquers and of the wheel acting one at the time and the test of their joint use. The level of residual disturbance torque acting on the platform after the balancing procedure requires the use of a stronger magnetic field with respect to the one present in a LEO. Augmenting the intensity of the magnetic field allows the magnetorquers to compensate for the gravity torque. For what concerns the wheel, this is used as a momentum wheel with a low bias rather than as a reaction wheel. Indeed, the motor used for the wheel is characterised by a highly nonlinear behaviour near the origin. After having tested the two types of actuators alone, the mixed magnetic/mechanical control has been tested. The control system shows good performance and low pointing error. However, the mechanical vibrations induced by the wheel cause a noisy signal for the magnetorquers dipole.

In section 6.1 the test of the magnetorquers for attitude control are reported. In section 6.2 the attitude control over one axis using the wheel is described. Finally, in Section 6.3 the results of the experimental test of the mixed magnetic/mechanical control are presented.

6.1 Magnetic attitude control

The magnetorquers play a pivotal role in the designed ACS. For this reason, pior to operations they have to be functionally tested. As a first approach, the Helmholtz Cage is set to generate a constant magnetic field in the vertical direction. As a consequence, the torque that can be generated by the interaction of the magnetorquers with the magnetic field lies in the horizontal plane. Hence, the magnetorquers are used to align the z axis of the body frame with the z axis of the inertial frame. The magnitude of the generated torque can be calculated as:

$$\|\boldsymbol{\tau}_{mag}\| = \|\mathbf{m}\|\|\mathbf{b}\| \tag{6.1}$$

As reported in Chapter 4, the intensity of the magnetic field present in orbit is $4 \times 10^{-5}T$, while the magnetorquers can provide a dipole up to $1Am^2$. Table resumes the difference between the condition present in a LEO and in the laboratory in terms of residual torques and magnetorquers performance in case they can provide a maximum dipole of $1Am^2$ under a magnetic field with intensity $3.7 \times 10^{-5}T$.

Environment:	**Orbit**	**Laboratory**
Main disturbance torque acting:	Magnetic torque	Gravity torque
Disturbance torque value:	$1.9 \times 10^{-5}Nm$	$1 \times 10^{-4}Nm$
Max magnetorquer torque:	$3.7 \times 10^{-5}Nm$	$3.7 \times 10^{-5}Nm$

Table 6.1: Comparision of disturbance torques and magnetorquers torque between the LEO and laboratory

Using the same magnetic field present in orbit, the magnitude of the control torque would not be sufficient to counteract the residual

unbalance torque. For this reason, in the experimental test of the magnetorquers, the intensity of the gravitational field generated by the HC is set equal to $6G = 6 \times 10^{-4}T$, leading to a maximum control torque of $6 \times 10^{-4}Nm$. Furthermore, it has been decided to generate a constant magnetic field. This was done for simplicity and removes the time-varying nature of the dynamics of a magnetic actuated spacecraft. The effects of neglecting the time-varying nature of the system are expected to be less severe for an equatorial orbit, for which the direction of the magnetic field is almost constant.

The magnetorquers have been tested using a control law aiming only to compensate for the component of the angular velocity perpendicular to the z axis and the attitude error in roll and pitch. The control torque is calculated as follows [9]:

$$\boldsymbol{\tau} = \boldsymbol{\tau}_p + \boldsymbol{\tau}_i + \boldsymbol{\tau}_\omega \tag{6.2}$$

where,

$$\boldsymbol{\tau}_p = -k_p \begin{bmatrix} \phi \\ \theta \\ 0 \end{bmatrix} \tag{6.3}$$

$$\boldsymbol{\tau}_i = -\frac{k_i}{K_p} \int_0^t \boldsymbol{\tau}_p dt \tag{6.4}$$

$$\boldsymbol{\tau}_\omega = -k_\omega (I - \hat{\mathbf{g}}\hat{\mathbf{g}}^T)\boldsymbol{\omega} \tag{6.5}$$

The desired dipole is then calculated as follows:

$$\mathbf{m} = \hat{b} \times \boldsymbol{\tau} \tag{6.6}$$

The gain chosen are reported in table 6.2. The results are shown in Fig. 6.1. Initial condition, steady-state value and settling time for the Euler angles are reported in table 6.3.

The magnetorquers have been also tested using the control law described by Eq. 4.1 by setting $k_{wh} = 0$. In this case, the weight matrix used are $Q_w = Q_q = 0.01 I_3$ (where I_3 is the 3x4 identity matrix) and $R = 10 I_3$. The resulting gain matrices are:

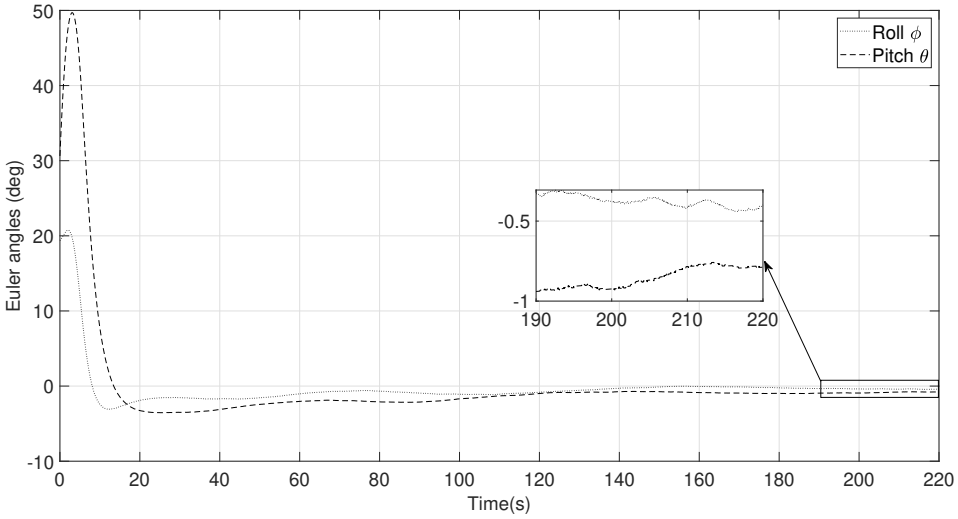

Figure 6.1: Time evolution of Euler angles during magnetic attitude PID control

k_p	k_i/k_p	k_ω
1.5	0.15	15

Table 6.2: Gain used for magnetic attitude PID control

$$D = \begin{bmatrix} 0.0359 & 0 & 0 \\ 0 & 0.0362 & 0 \\ 0 & 0 & 0.0347 \end{bmatrix} \quad K = \begin{bmatrix} 0.0316 & 0 & 0 \\ 0 & 0.0316 & 0 \\ 0 & 0 & 0.0316 \end{bmatrix} \tag{6.7}$$

The gain matrices are practically approximated by $D = K = 0.03 I_3$. Fig. 6.2 shows the result in terms of Euler angles while Tab 6.4 shows initial condition, steady-state value and settling time. Both cases show that the torque provided by the interaction between the magnetorquers and the external magnetic field is sufficient to compensate for the disturbance torques.

Euler angle	**Initial value**	**Steady value**	**Settling time**
Roll ϕ	19.39°	0.40°	53s
Pitch θ	30.63°	0.82°	36s

Table 6.3: Initial condition, steady value and settling time for the Euler angle during magnetic attitude PID control

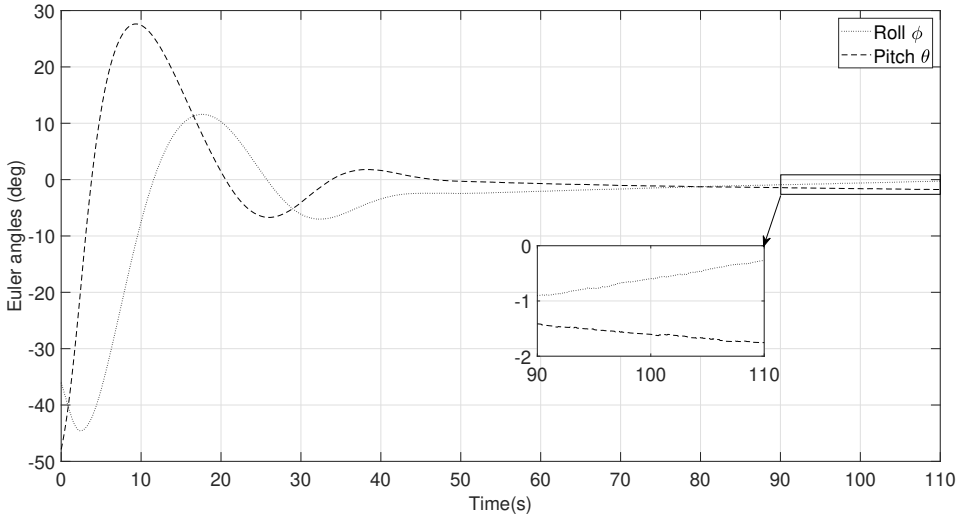

Figure 6.2: Time evolution of Euler angles during magnetic attitude LQR control

Euler angle	**Initial value**	**Steady value**	**Settling time**
Roll ϕ	$-36°$	0.63°	44s
Pitch θ	$-47°$	1.58°	44s

Table 6.4: Initial condition, steady value and settling time for the Euler angle during magnetic attitude LQR control

6.2 Attitude control using the wheel

The wheel is tested in its capacity to provide control over one axis. In order to minimise the angular velocity components in the horizontal plane, the vertical moving mass position is brought to its lowest value. A simple PID law is used for calculating the desired torque around the z axis. Then the torque to be actuated by the wheel is calculated assuming that the angular velocity is parallel to the z axis. In that case, Eq. 3.8 reduces to Eq. 5.2, here reported.

$$J_z \omega_z = -\dot{h} \tag{6.8}$$

Since the wheel is controlled in velocity (by providing the reference signal by Pulse Width Modulation), the desired torque cannot be commanded directly. Hence, the reference speed is calculated by numerically integrate the desired torque:

$$\Omega_w(k+1) = \Omega_w(k) + \frac{\delta t}{J_w}\dot{h} \tag{6.9}$$

where δt was the sampling time equal to $0.05s$. Because of the nonlinear behaviour of the motor near the origin, this is not used as a proper reaction wheel but rather as a momentum wheel with a low bias. In particular, in this test, the initial velocity of the wheel is set equal to $1000rpm$. Fig. 6.3 shows the result of the attitude control over one axis, while Tab. 6.5 reports initial condition, with steady-state error and settling time.

Euler angle	**Initial value**	**Steady value**	**Settling time**
Yaw γ	$-123.47°$	$0.29°$	$82s$

Table 6.5: Initial condition, steady value and settling time for the Yaw angle during wheel control

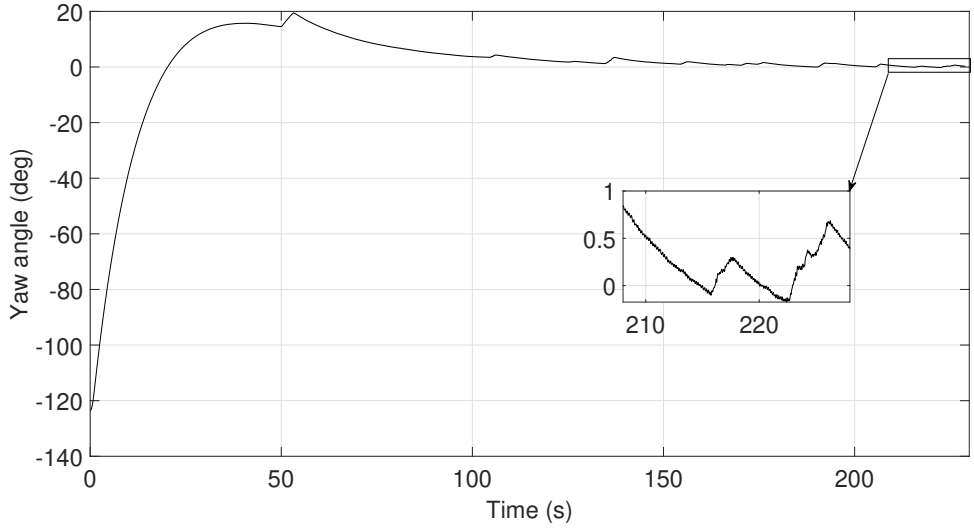

(a)

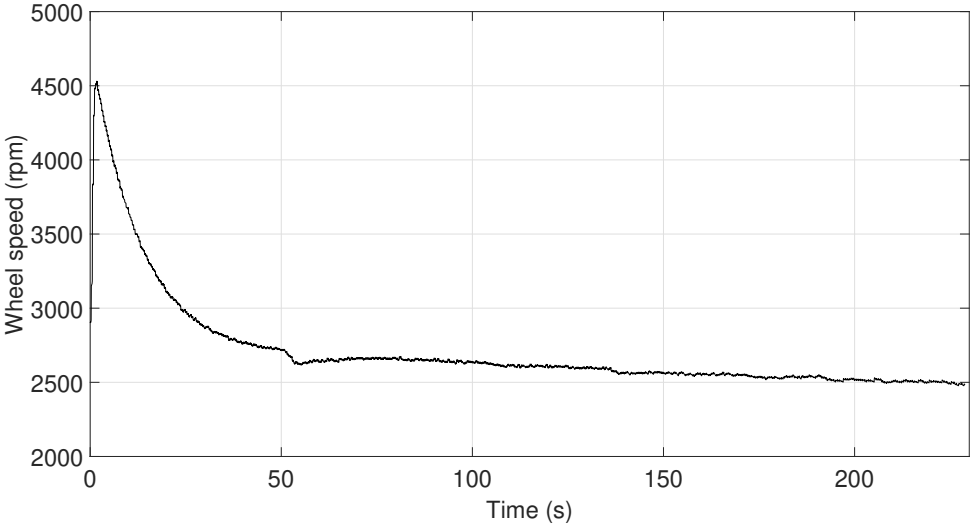

(b)

Figure 6.3: Yaw angle (a) and wheel speed (b) during attitude control using the wheel

6.3 Mixed magnetic/mechanical attitude control

The mixed magnetic/mechanical actuation, already introduced in the Chapter 4, is tested on the real hardware for an inertial pointing. The Helmholtz cage is set to generate a constant magnetic field parallel to the local vertical. This scenario is similar to the one of a satellite in LEO since in that case the magnetic field is almost constant and perpendicular to the orbital plane. In Section 6.1 it has been shown how using a magnetic field exactly equal to the one present in orbit would not allow the magnetorquers to compensate for the gravity torque. For this reason, the magnetic field intensity is set to $6 \times 10^{-4} T$. The wheel is used as a momentum wheel with a low bias due to the nonlinear behaviour of the motor at low speed. Using a momentum wheel adds gyro properties to the satellite and helps compensating for the disturbance torques. At the same time, it requires a greater control action of the magnetorquers in controlling the orientation of the spacecraft axis parallel to the wheel axis. The value of the bias is chosen as a compromise between avoiding exceedingly low speed for the motor during the control and limiting the momentum bias. The residual disturbance torque acting on the platform during the tests and the actuators characteristics are resumed in Table 6.6.

Parameter	Symbol	Value	Units
Gravity torque	τ_g	1.4×10^{-4}	Nm
Magnetic field norm	$\|\mathbf{b}\|$	6×10^{-4}	T
Wheel moment of inertia	J_w	8171.43×10^{-9}	Kgm^2
Wheel momentum bias	h_0	4.2786×10^{-4}	Nms
Maximum magnetic dipole	$\mathbf{m}_{max}$	1	Am^2
Maximum magnetorquers torque	$\tau_{m,max}$	3.7×10^{-5}	Nm

Table 6.6: Disturbance torques and actuators characteristics, mixed magnetic/mechanical control

The required control torque is calculated according to Section 4.1.

The weight matrices for the LQR are set equal to $Q_w = Q_q = 0.01I_3$ (where I_3 is the 3x4 identity matrix) and $R = 0.25I_3$. The resulting D and K matrices are approximated to $0.2I_3$. The control torque is then distributed between the wheel and the magnetorquers by using Eq. 4.1. The gain k_{wh} scaling the torque commanded to the wheel is set equal to 0.1 and 1 in order to show its effect on the wheel speed. In Table 6.7 initial conditions, steady-state value and settling time are reported for the two cases. The Euler angles and the wheel speed are shown in Fig 6.5 for $k_{wh} = 0.1$ and in Fig. 6.7 for $k_{wh} = 1$ while the commanded dipoles are shown respectively in Fig. 6.4 and 6.6. The wheel speed present more abrupt changes in the case $k_{wh} = 1$ but the steady state attitude error is lower than what achieved with $k_{wh} = 0.1$. This suggests that further investigations may be undertaken on the controller gain tuning for enhancing the performance

Euler angle	**Initial value**	**Steady value**	**Settling time**
	$k_{wh} = 0.1$		
Roll ϕ	$45.23°$	$0.35°$	$26s$
Pitch θ	$1.86°$	$0.87°$	$29s$
Yaw γ	$-149.57°$	$1.9°$	$15s$
	$k_{wh} = 1$		
Roll ϕ	$23.81°$	$0.05°$	$12s$
Pitch θ	$35.33°$	$0.8°$	$3s$
Yaw γ	$-43.04°$	$0.45°$	$12s$

Table 6.7: Initial condition, steady value and settling time for mixed magnetic/mechanical attitude control in the case $k_{wh} = 0.1$ and $k_{wh} = 1$

The magnetorquers dipoles show very noisy behaviour. This was found to be caused by the mechanical vibration of the wheel that introduced additional noise on the gyroscopes reading. This fact can be noted in Fig. 6.8 where the angular velocity data from the gyroscopes is shown at different wheel speeds. The mechanical vibration become important already after 1000 rpm. Future work should consider a better mounting of the wheel, maybe through conical coupling or the

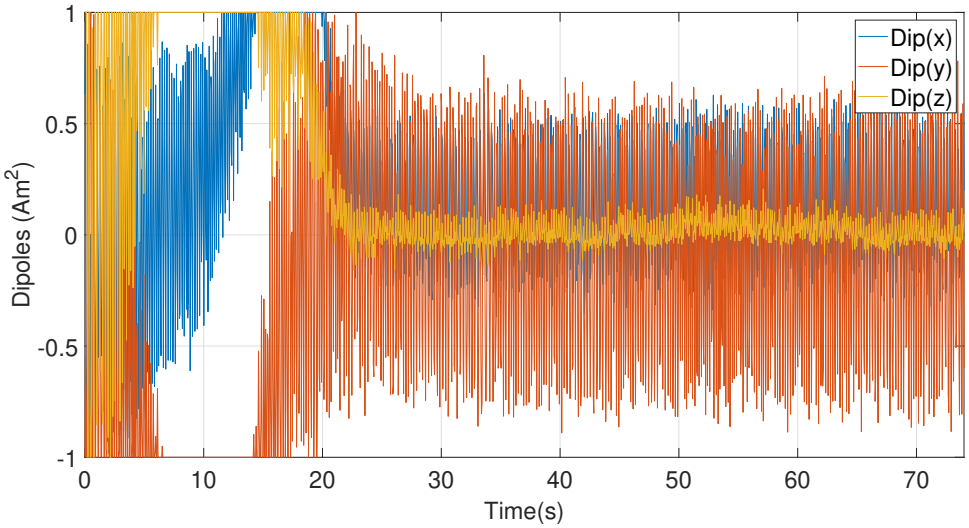

Figure 6.4: Magnetorquers dipoles during mixed magnetic/mechanical control with $k_{wh} = 0.1$

implementation of a on board low-pass filter for the gyroscope data.

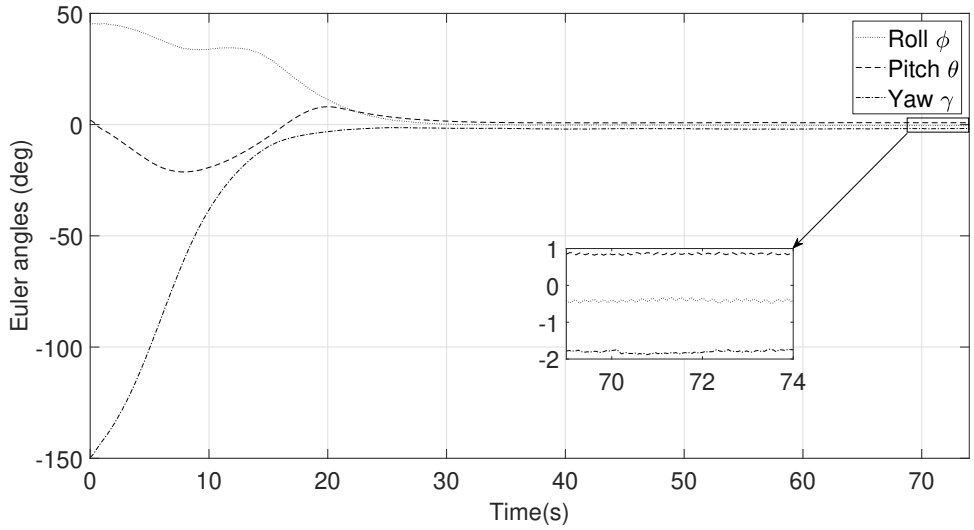

(a)

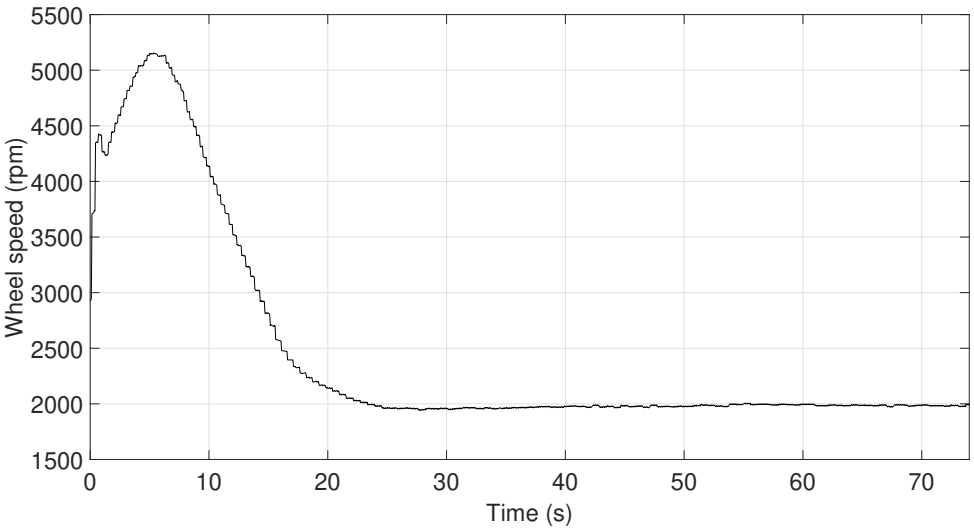

(b)

Figure 6.5: Euler angles (a) and wheel speed (b) during mixed magnetic/mechanical control with $k_{wh} = 0.1$

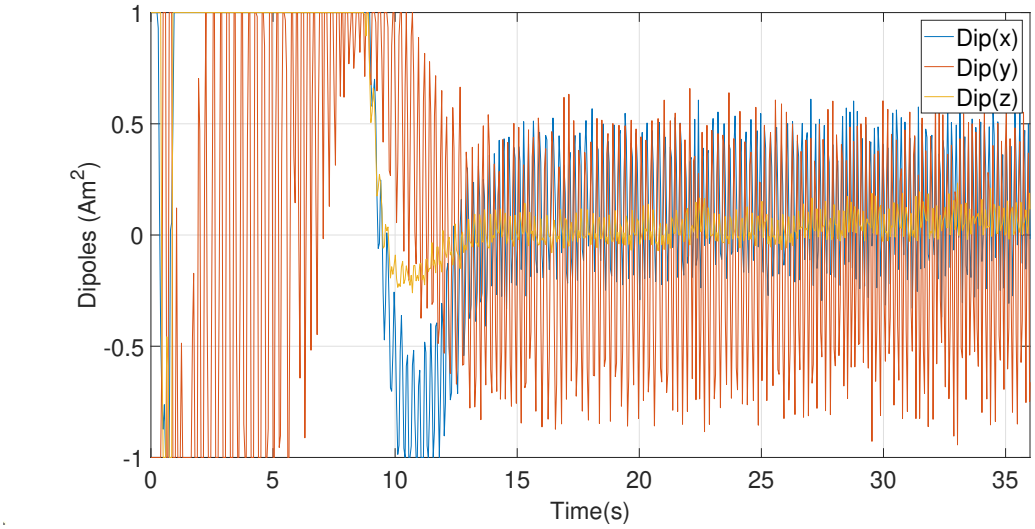

Figure 6.6: Magnetorquers dipoles during mixed magnetic/mechanical control using $k_{wh} = 1$

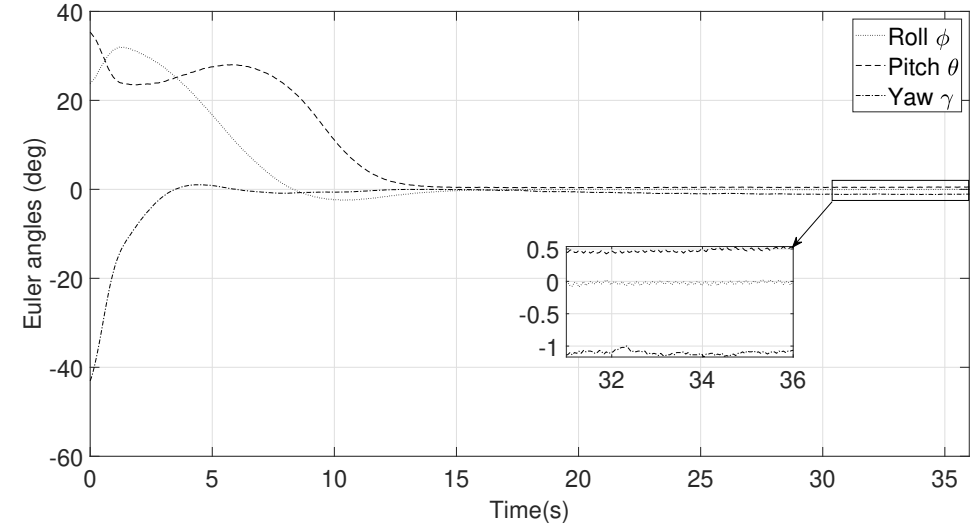

(a)

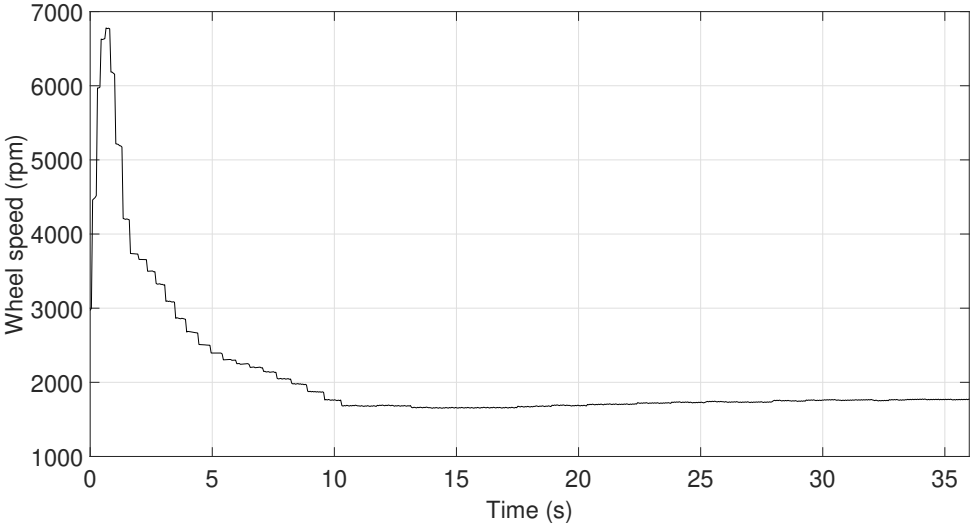

(b)

Figure 6.7: Euler angles (a) and wheel speed (b) during mixed magnetic/mechanical control with $k_{wh} = 1$

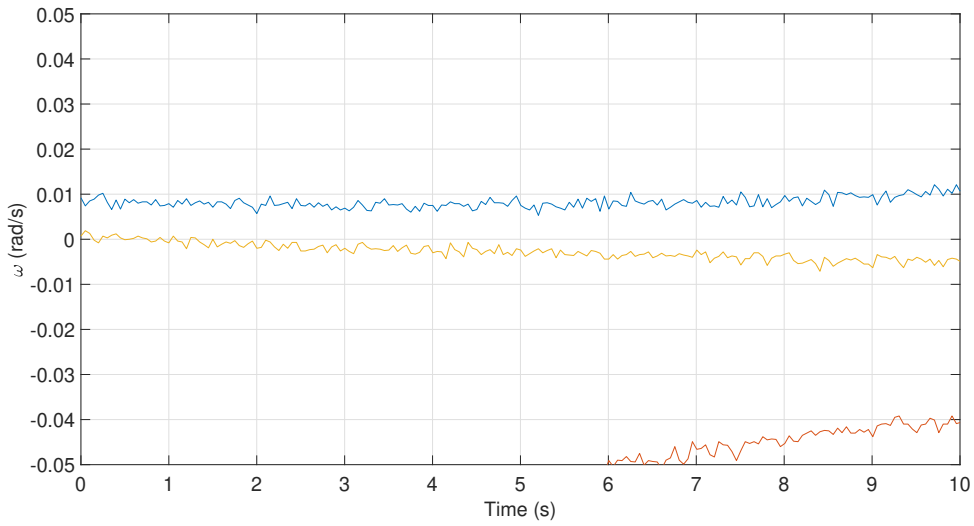
0.05
0.04
0.03
0.02
0.01
0
-0.01
-0.02
-0.03
-0.04
-0.05
ω (rad/s)
0
1
2
3
4
5
6
7
8
9
10
Time (s)

(a)

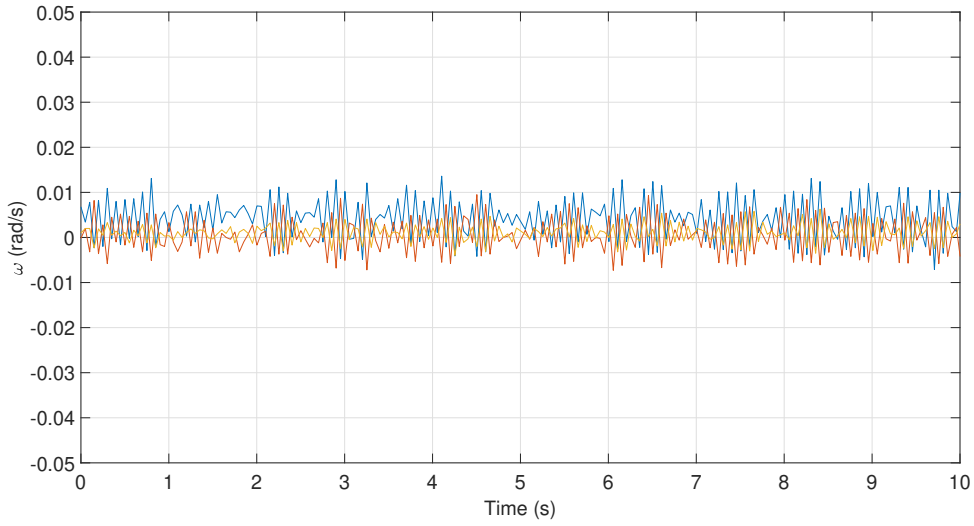
0.05
0.04
0.03
0.02
0.01
0
-0.01
-0.02
-0.03
-0.04
-0.05
ω (rad/s)
0
1
2
3
4
5
6
7
8
9
10
Time (s)

(b)

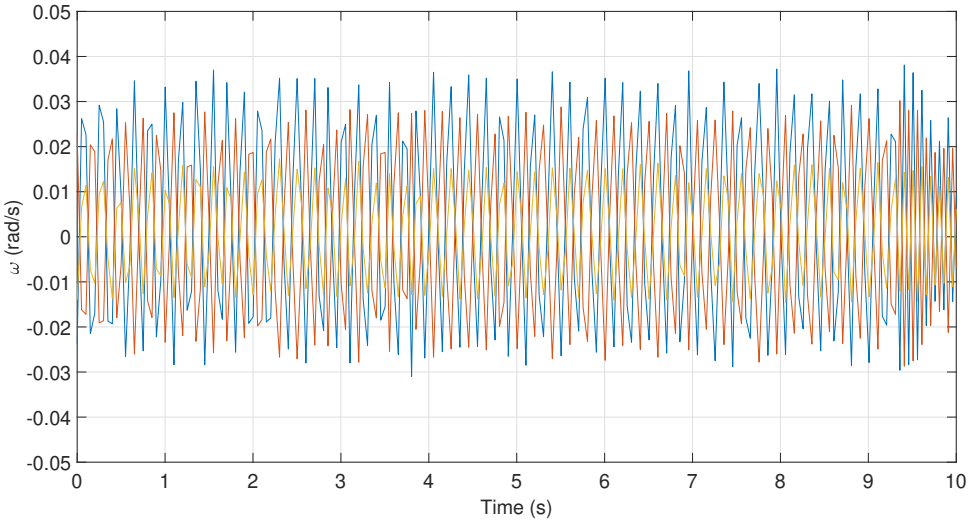

(c)

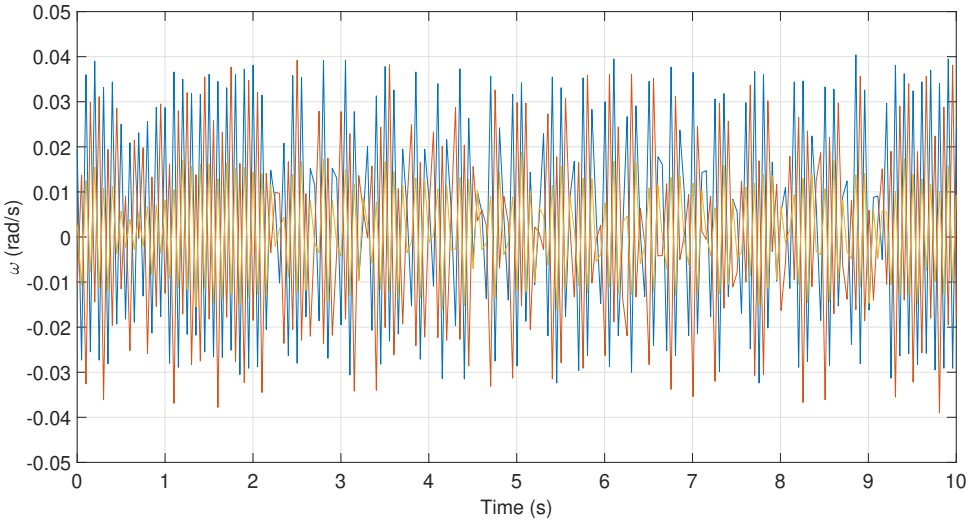

(d)

Figure 6.8: Gyroscope data at different wheel speed: (a) 0 rpm (b) 1000 rpm (c) 3000 rpm (d) 8000 rpm

Conclusions

The work done in this thesis tackled the problem of attitude control for nanosatellites employing magnetic and mechanical actuators. Magnetorquers are often employed thanks to their reduced dimensions and the smoothness of application. However, their performance are limited from their intrinsic underactuation in the direction parallel to the external magnetic field. Reaction wheels, on the other hand, offer better performance but are prone to failure and must be periodically desaturated. In order to overcome the limits of the magnetorquers and still maintaining a compact system, a control system employing three magnetorquers and a reaction wheel has been studied. These two systems had to be integrated together to provide three-axis control.

In the first part of the thesis, bibliographic research on how these two systems could be used together was conducted. The most promising approach consisted of a geometric distribution of the torque between the magnetorquers and the reaction wheel. Parametric studies were conducted in order to understand which orbit and wheel design configurations offered the best performance. It was then decided to mount the wheel on the third axis and consider an equatorial orbit. The control redistribution law was used in conjunction with a LQR controller. To the best of the author's knowledge, despite their simplicity, there were no examples of this approach being applied with linear control techniques. Realistic simulations, tuned for a spacecraft of a nanosatellite class were conducted. The stability of the control approach with respect to parameters variations was shown by means of Monte-Carlo approach.

In the second part of the thesis, the designed attitude control system

was tested on an attitude simulator testbed at the University of Bologna. Testing required the compensation of the main disturbance torques acting on the platform. The gravity torque was compensated using an automatic mass balancing system together with magnetorquers for angular velocity damping. The residual torque was reduced to value on the order of $10^{-4}Nm$. This value of torque required the use of a stronger magnetic field compared to the one encountered by a spacecraft in a low Earth orbit. After magnetic and mechanical subsystem separate testing, the designed control approach was applied to a nanosatellite of 1U class. The simulations and the tests showed that the use of mixed magnetic/mechanical control is effective in providing high accuracy in three-axis attitude control.

Future work should enhancing the performance of the control system and validate it with even more realistic scenarios. The commanded dipoles showed a noisy behaviour and this has been attributed to the mechanical vibrations caused by the wheel. It should be considered to reduce the effect of wheel mechanical vibrations. This could be done with with an improved wheel assembly or in the form of an onboard low-pass filter for the gyroscopes data. Furthermore, the wheel motor showed a highly nonlinear behaviour near the origin and this fact forced its use as a momentum wheel with very low bias rather than a reaction wheel. Future work should consider replacing the motor with a more performing one. Also, in this work, the magnetic field was constant and parallel to the local vertical. It could be interesting to use a more realistic time-varying magnetic field, like the one encountered in orbit. Finally, the joint use of shifting masses and magnetorquers showed a potential for enhanced performance of the automatic balancing system. This approach could be further investigated in future work.

Bibliography

[1] E. Kulu, "Nanosats database." Available at `https://www.nanosats.eu/`.

[2] X. Li, S. Palo, R. Kohnert, D. Gerhardt, L. Blum, Q. Schiller, D. Turner, W. Tu, N. Sheiko, and C. S. Cooper, *Colorado Student Space Weather Experiment: Differential Flux Measurements of Energetic Particles in a Highly Inclined Low Earth Orbit*, pp. 385–404. American Geophysical Union (AGU), 2012.

[3] J. L. Schwartz, M. A. Peck, and C. D. Hall, "Historical review of air-bearing spacecraft simulators," *Journal of Guidance, Control, and Dynamics*, vol. 26, no. 4, pp. 513–522, 2003.

[4] M. N. Sweeting, "Modern small satellites-changing the economics of space," *Proceedings of the IEEE*, vol. 106, no. 3, pp. 343–361, 2018.

[5] T. Villela, C. Costa, A. Brandão, F. Bueno, and R. Leonardi, "Towards the thousandth cubesat: A statistical overview," *International Journal of Aerospace Engineering*, vol. 2019, pp. 1–13, jan 2019.

[6] H. Polat, J. Virgili-Llop, and M. Romano, "Survey, statistical analysis and classification of launched cubesat missions with emphasis on the attitude control method," *Journal of Small Satellites*, vol. 5, pp. 513–530, jan 2016.

[7] P. Puig-suari, C. Turner, and R. Twiggs, "Cubesat: The development and launch support infrastructure for eighteen different satellite customers on one launch," in *15TH Annual/USU Conference on Small Satellites*, jan 2001.

[8] I. Gavrilovich, S. Krut, M. Gouttefarde, F. Pierrot, and L. Dusseau, "Robotic test bench for cubesat ground testing: Concept and satellite dynamic parameter identification," in *2015 IEEE/RSJ International Conference on Intelligent Robots and Systems (IROS)*, pp. 5447–5453, 2015.

[9] A. Bahu, *Development of a ground testing facility and attitude control for magnetically actuated nanosatellites*. PhD thesis, University of Bologna, may 2021.

[10] D. Modenini, A. Bahu, G. Curzi, and A. Togni, "A dynamic testbed for nanosatellites attitude verification," *Aerospace*, vol. 7, no. 3, 2020.

[11] A. Mody, T. Sharma, P. Tekriwal, G. Subramanian, A. Ratheesh, and K. Barad, "Attitude determination and control system design for srmsat-2: A micro class lunar orbiter," in *55th AIAA Aerospace Sciences Meeting, AIAA SciTech 2017*, jan 2017.

[12] S. Bhat, "Controllability of nonlinear time-varying systems: applications to spacecraft attitude control using magnetic actuation," *IEEE Transactions on Automatic Control*, vol. 50, no. 11, pp. 1725–1735, 2005.

[13] S. Bhat and A. Dham, "Controllability of spacecraft attitude under magnetic actuation," in *42nd IEEE International Conference on Decision and Control (IEEE Cat. No.03CH37475)*, vol. 3, pp. 2383–2388 Vol.3, 2003.

[14] M. Y. Ovchinnikov and D. Roldugin, "A survey on active magnetic attitude control algorithms for small satellites," *Progress in Aerospace Sciences*, vol. 109, p. 100546, 2019.

[15] E. de Angelis, F. Giulietti, A. Ruiter, and G. Avanzini, "Spacecraft attitude control using magnetic and mechanical actuation," *Journal of Guidance, Control, and Dynamics*, vol. 39, pp. 1–10, nov 2015.

[16] Y. Yang, *Spacecraft Modeling, Attitude Determination, and Control Quaternion-based Approach*. Rockville, Maryland, USA: US Nuclear Regulatory Commission Office of Research, 2002.

[17] C. Damaren, "Hybrid magnetic attitude control gain selection," *Proceedings of The Institution of Mechanical Engineers Part G-journal of Aerospace Engineering - PROC INST MECH ENG G-J A E*, vol. 223, pp. 1041–1047, dec 2009.

[18] Y. Kim, *Resolving Radrasat-1 Momentum Wheel Failure Problem*. American Institute of Aeronautics and Astronautics, 2003.

[19] J. Forbes and C. Damaren, "Geometric approach to spacecraft attitude control using magnetic and mechanical actuation," *Journal of Guidance Control and Dynamics*, vol. 33, pp. 590–595, mar 2010.

[20] L. Markley and J. Crassidis, *Fundamentals of Spacecraft Attitude Determination and Control*. Springer Verlag, jan 2014.

[21] J. R. Wertz, *Spacecraft Attitude Determination and Control*. KLUWER ACADEMIC PUBLISHERS, 2002.

[22] "Nrlmsise-00 atmosphere model." Available at `https://ccmc.gsfc.nasa.gov/modelweb/models/nrlmsise00.php`.

[23] V. Beletskii, "Motion of an artificial satellite about its center of mass." Available at `https://archive.org/details/nasa_techdoc_19670006100`, jan 1966.

[24] "Dipole approximations of the geomagnetic field." Available at `https://www.spenvis.oma.be/help/background/magfield/cd.html`.

[25] M. R. Brewer, "Cubesat attitude determination and helmholtz cage design," Master's thesis, Air Force Institute of Technology, 2012.

[26] G. A. Smith, "Dynamic simulators for test of space vehicle attitude control systens," in *Proceedings of the Conference on the Role of Simulation in Space Technology*, p. XV– 1–XV–30, 1964.

[27] S. Chesi, Q. Gong, V. Pellegrini, R. Cristi, and M. Romano, "Automatic mass balancing of a spacecraft three-axis simulator: Analysis and experimentation," *Journal of Guidance, Control, and Dynamics*, vol. 37, no. 1, pp. 197–206, 2014.

[28] J. R. Forbes, *Extensions of Input-Output Stability Theory and the Control of Aerospace Systems*. PhD thesis, University of Toronto, 2011.

[29] M. Reyhanoglu and J. Rubio-Hervas, "Three-axis magnetic attitude control algorithms for small satellites," in *RAST 2011 - Proceedings of 5th International Conference on Recent Advances in Space Technologies*, pp. 897 – 902, jul 2011.

[30] M. Lovera and A. Astolfi, "Global magnetic attitude control of spacecraft in the presence of gravity gradient," *IEEE Transactions on Aerospace and Electronic Systems*, vol. 42, no. 3, pp. 796–805, 2006.

[31] P. A. Capo-Lugo, J. Rakoczy, and D. Sanders, "The b-dot earth average magnetic field," *Acta Astronautica*, vol. 95, pp. 92–100, 2014.

[32] J. S. White, F. H. Shigemoto, and K. Bourquin, "Satellite attitude control utilizing the earth's magnetic field," tech. rep., Ames Research Center, Moffet Field, California, aug 1961.

[33] P. Camillo and L. Markley, "Orbit-averaged behavior of magnetic control laws for momentum unloading," *Journal of Guidance, Control, and Dynamics*, vol. 3, jan 1981.

[34] G. Avanzini and F. Giulietti, "Magnetic detumbling of a rigid spacecraft," *Journal of Guidance, Control, and Dynamics*, vol. 35, no. 4, pp. 1326–1334, 2012.

[35] A. C. Stickler and K. Alfriend, "Elementary magnetic attitude control system," *Journal of Spacecraft and Rockets*, vol. 13, no. 5, pp. 282–287, 1976.

[36] M. Lovera and A. Astolfi, "Spacecraft attitude control using magnetic actuators," *Automatica*, vol. 40, no. 8, pp. 1405–1414, 2004.

[37] F. Schiavo, M. Lovera, and A. Astolfi, "Magnetic attitude control of spacecraft with flexible appendages," in *Proceedings of the 45th IEEE Conference on Decision and Control*, pp. 1545–1550, 2006.

[38] T. Pulecchi and M. Lovera, "Attitude control of spacecraft with partially magnetic actuation," *IFAC Proceedings Volumes*, vol. 40, no. 7, pp. 609–614, 2007. 17th IFAC Symposium on Automatic Control in Aerospace.

[39] J. R. Forbes and C. J. Damaren, "Linear time-varying passivity-based attitude control employing magnetic and mechanical actuation," *Journal of Guidance, Control, and Dynamics*, vol. 34, no. 5, pp. 1363–1372, 2011.

[40] J. Guo and C. Han, "Where is the limit: The analysis of cubesat adcs performance," in *Small Satellites, System & Services Symposium (4S)*, may 2016.

[41] N. Chaturvedi, F. Bacconi, D. Bernstein, and N. McClamroch, "Stabilization of a 3d axially symmetric rigid pendulum," in *Proceedings of the 44th IEEE Conference on Decision and Control*, pp. 5287–5292, 2005.